Horn, A., N. Li, T. A. Dembek, A. Kappel, C. Boulay, S. Ewert, A. Tietze, A. Husch, T. Perera, W. J. Neumann, M. Reisert, H. Si, R. Oostenveld, C. Rorden, F. C. Yeh, Q. Fang, T. M. Herrington, J. Vorwerk, and A. A. Kuhn. 2019. Lead-DBS v2: Towards a comprehensive pipeline for deep brain stimulation imaging. *Neuroimage*. **184**: 293-316.

doi: 10.1016/j.neuroimage.2018.08.068

Title

Lead-DBS v2: Towards a comprehensive pipeline for deep brain stimulation imaging

Authors

Andreas Horn[1*], Ningfei Li[1*], Till A Dembek[2], Ari Kappel[3], Chadwick Boulay[4], Siobhan Ewert[1], Anna Tietze[5], Andreas Husch[6], Thushara Perera[7,8], Wolf-Julian Neumann[1,5], Marco Reisert[9], Hang Si[10], Robert Oostenveld[11,12], Christopher Rorden[13], Fang-Cheng Yeh[14], Qianqian Fang[15], Todd M Herrington[16], Johannes Vorwerk[17], Andrea A. Kühn[1]

Author Affiliations

1. Movement Disorders & Neuromodulation Unit, Department for Neurology, Charité – University Medicine Berlin, Germany
2. Department of Neurology, University Hospital of Cologne, Germany
3. Wayne State University, Department of Neurosurgery
4. Ottawa Hospital Research Institute
5. Institute of Neuroradiology, Charité – University Medicine Berlin, Germany
6. University of Luxembourg, Luxembourg Centre for Systems Biomedicine, Interventional Neuroscience Group, Belvaux, Luxembourg
7. Bionics Institute, East Melbourne, Victoria, Australia
8. Department of Medical Bionics, University of Melbourne, Parkville, Victoria, Australia
9. Medical Physics, Department of Radiology, Faculty of Medicine, University Freiburg, Germany
10. Numerical Mathematics and Scientific Computing, Weierstrass Institute for Applied Analysis and Stochastics (WIAS)
11. Donders Institute for Brain, Cognition and Behaviour, Radboud University, Nijmegen, NL
12. NatMEG, Karolinska Institutet, Stockholm, SE
13. McCausland Center for Brain Imaging, University of South Carolina, Columbia, SC, USA.
14. Department of Neurological Surgery, University of Pittsburgh PA, USA
15. Department of Bioengineering, Northeastern University, Boston, USA
16. Department of Neurology, Massachusetts General Hospital, Harvard Medical School, Boston, MA. USA.
17. Scientific Computing & Imaging (SCI) Institute, University of Utah, Salt Lake City, USA

* Authors contributed equally

Corresponding Author

Dr. Andreas Horn
Movement Disorders & Neuromodulation Unit
Department for Neurology
Charité – University Medicine Berlin
Charitéplatz 1, 10117 Berlin, Germany
E-mail: andreas.horn@charite.de

List of abbreviations

ANTs	Advanced Normalization Tools, see http://stnava.github.io/ANTs/
BSpline-SyN	ANTs normalization method; Explicit B-spline regularization in symmetric diffeomorphic image registration
CORE	Algorithm for “reconstruction of electrode contact positions” defined in Horn & Kühn 2014
DARTEL	SPM normalization method; A fast diffeomorphic image registration algorithm.
DiODe	Directional Orientation Detection (Sitz et al. 2017)
dMRI	Diffusion-weighted MRI – in the context of diffusion-imaging based tractography.
FA	Fractional Anisotropy
FGATIR	Fast Grey Matter Acquisition T1 Inversion Recovery
FLIRT	FMRIB's Linear Image Registration Tool
FNIRT	FSL normalization method; FMRIB's Nonlinear Image Registration Tool
FSL	FMRIB Software Library, see https://fsl.fmrib.ox.ac.uk/
GNU	Recursive acronym for “GNU's Not Unix.”; GNU GPL is a popular open license supported by the Free Software Foundation (see http://www.gnu.org). The Free Software Foundation (FSF) is a nonprofit with a worldwide mission to promote computer user freedom.
GPi	internal segment of the globus pallidus
GPe	external segment of the globus pallidus
GQI	Generalized q-sampling imaging, dMRI processing method implemented in DSI studio
HCP	Human Connectome Project
LEDD	Levodopa Equivalent Daily Dosage
MAGeT Brain	Multiple Automatically Generated Templates brain segmentation algorithm, see https://github.com/CobraLab/MAGeTbrain
PaCER	Precise and Convenient Electrode Reconstruction for DBS, see https://adhusch.github.io/PaCER/
PCA	Principal Component Analysis
PPMI	Parkinson‘s Disease Progression Marker Initiative
PPN	Pedunculopontine nucleus
RN	red nucleus
ROI	Region of Interest
RSME	Root-mean-square error
QSM	Quantitative Susceptibility Mapping
rs-fMRI	Resting-state functional MRI
SHOOT	SPM normalization method; Diffeomorphic registration using geodesic shooting and Gauss–Newton optimisation
SPM	Statistic Parametric Mapping, see http://www.fil.ion.ucl.ac.uk/spm/software/spm12/
STN	subthalamic nucleus
SyN	ANTs normalization method; Symmetric diffeomorphic image registration / symmetric image normalization
TRAC	Algorithm for “trajectory reconstruction” defined in Horn & Kühn 2014
UPDRS	Unified Parkinson‘s Disease Rating Scale
VTA	Volume of Tissue Activated

Abstract

Deep brain stimulation (DBS) is a highly efficacious treatment option for movement disorders and a growing number of other indications are investigated in clinical trials. To ensure optimal treatment outcome, exact electrode placement is required. Moreover, to analyze the relationship between electrode location and clinical results, a precise reconstruction of electrode placement is required, posing specific challenges to the field of neuroimaging. Since 2014 the open source toolbox Lead-DBS is available, which aims at facilitating this process. The tool has since become a popular platform for DBS imaging. With support of a broad community of researchers worldwide, methods have been continuously updated and complemented by new tools for tasks such as multispectral nonlinear registration, structural / functional connectivity analyses, brain shift correction, reconstruction of microelectrode recordings and orientation detection of segmented DBS leads. The rapid development and emergence of these methods in DBS data analysis require us to revisit and revise the pipelines introduced in the original methods publication.

Here we demonstrate the updated DBS and connectome pipelines of Lead-DBS using a single patient example with state-of-the-art high-field imaging as well as a retrospective cohort of patients scanned in a typical clinical setting at 1.5T. Imaging data of the 3T example patient is co-registered using five algorithms and nonlinearly warped into template space using ten approaches for comparative purposes. After reconstruction of DBS electrodes (which is possible using three methods and a specific refinement tool), the volume of tissue activated is calculated for two DBS settings using four distinct models and various parameters. Finally, four whole-brain tractography algorithms are applied to the patient‘s preoperative diffusion MRI data and structural as well as functional connectivity between the stimulation volume and other brain areas are estimated using a total of eight approaches and datasets. In addition, we demonstrate impact of selected preprocessing strategies on the retrospective sample of 51 PD patients. We compare the amount of variance in clinical improvement that can be explained by the computer model depending on the method of choice.

This work represents a multi-institutional collaborative effort to develop a comprehensive, open source pipeline for DBS imaging and connectomics, which has already empowered several studies, and may facilitate a variety of future studies in the field.

Introduction

In the field of deep brain stimulation (DBS), precise electrode placement is crucial for optimal treatment outcomes. Specifically, a direct relationship between electrode localization and clinical outcome has been shown in multiple studies (e.g. Butson et al., 2011; Dembek et al., 2017; Eisenstein et al., 2014; Garcia-Garcia et al., 2016; Horn et al., 2017c; Mosley et al., 2018b; also see fig. 1 A). To characterize this relationship in an objective manner, tools are required that facilitate the reconstruction of electrode placement such that comparisons between patients can be made. Group comparisons play a crucial role in identifying optimal electrode placement, providing both direct clinical and theoretical insights. Ideally, to fulfill reproducibility and transparency criteria needed for good scientific practice, these tools should be open source and publicly available. Finally, a specific challenge that differentiates the field of DBS imaging from most other neuroimaging domains is the need for absolute anatomical precision. A shift of two mm in electrode placement may represent a major change in clinical outcome, while in conventional fMRI studies, a change of an activity peak by two mm has little if no impact at all (figure 1).

In 2014, the software toolbox Lead-DBS was published that aimed at reconstructing DBS electrode placement based on pre- and postoperative imaging (Horn and Kühn, 2015; www.lead-dbs.org; RRID:SCR_002915). Using the toolbox, electrodes may be localized in relationship to surrounding brain anatomy. Since its initial publication, development efforts have continued at multiple institutions. Thus, over the years, numerous progress has been made and better alternatives for most steps described in the original pipeline are now provided (Ewert et al., 2018a; 2018b; Horn et al., 2017a; 2017b; 2017c). Moreover, several novel features that were not mentioned (or available) in the original publication have recently become crucial components of DBS imaging. These have now been integrated in the latest release. While other tools with similar aims have been introduced after publication of Lead-DBS (Bonmassar et al., 2014; da Silva et al., 2015; D'Albis et al., 2014; Husch et al., 2017; 2018; Lauro et al., 2015), the tool was recently described as the most established toolbox for electrode localizations (Husch et al., 2017) with over 6600 downloads and 75 citations. The aim of the project is to develop a scientific platform in a multi-institutional endeavor that is and remains available under an open license (GNU general public license v. 3) to ensure reproducibility and version control.

The growing user base of Lead-DBS as an academic toolbox and the divergence of the current methods and those described in the initial publication raise the need of an updated

methodological pipeline description. In addition, we also use the opportunity to emphasize the latest default analysis options, pitfalls and methods throughout the pipeline.

Given the complexity of multiple processing stages (see figure 2 & tables 1-4), a thorough empirical evaluation of each stage exceeds the scope of this work. For instance, it would represent a study in itself to empirically probe which normalization method, which stimulation volume model or which fiber tracking approach could yield best results. Such studies have been conducted (Åström et al., 2014; Dembek et al., 2017; Fillard et al., 2011; Klein et al., 2009; Maier-Hein et al., 2017; McIntyre et al., 2004) and are currently underway in context of the Lead-DBS environment, as well (Ewert et al., 2018a). Instead, the aim of the present article is to give an overview of methods available in Lead-DBS. To make the processing stages concrete, the pipeline is described using a single patient example with state-of-the art high-field (3T) imaging as well as a retrospective sample of 51 PD patients imaged at 1.5T. The result is a focus on the methods section and a descriptive results section covering co-registration, normalization, electrode localization, VTA estimation, and structural-functional connectivity analyses. Finally, we demonstrate that more variance in clinical outcome may be explained when using the default pipeline in comparison to a more “standard neuroimaging” approach. The manuscript has a narrative prose with the aim of maximizing understandability while omitting unnecessary details where possible. Moreover, while the manuscript is still structured into conventional sections, the methods descriptions exceed the actual processing of the study with the aim of illustrating the multiple approaches implemented in Lead-DBS and providing notes about motivation and potential limitations.

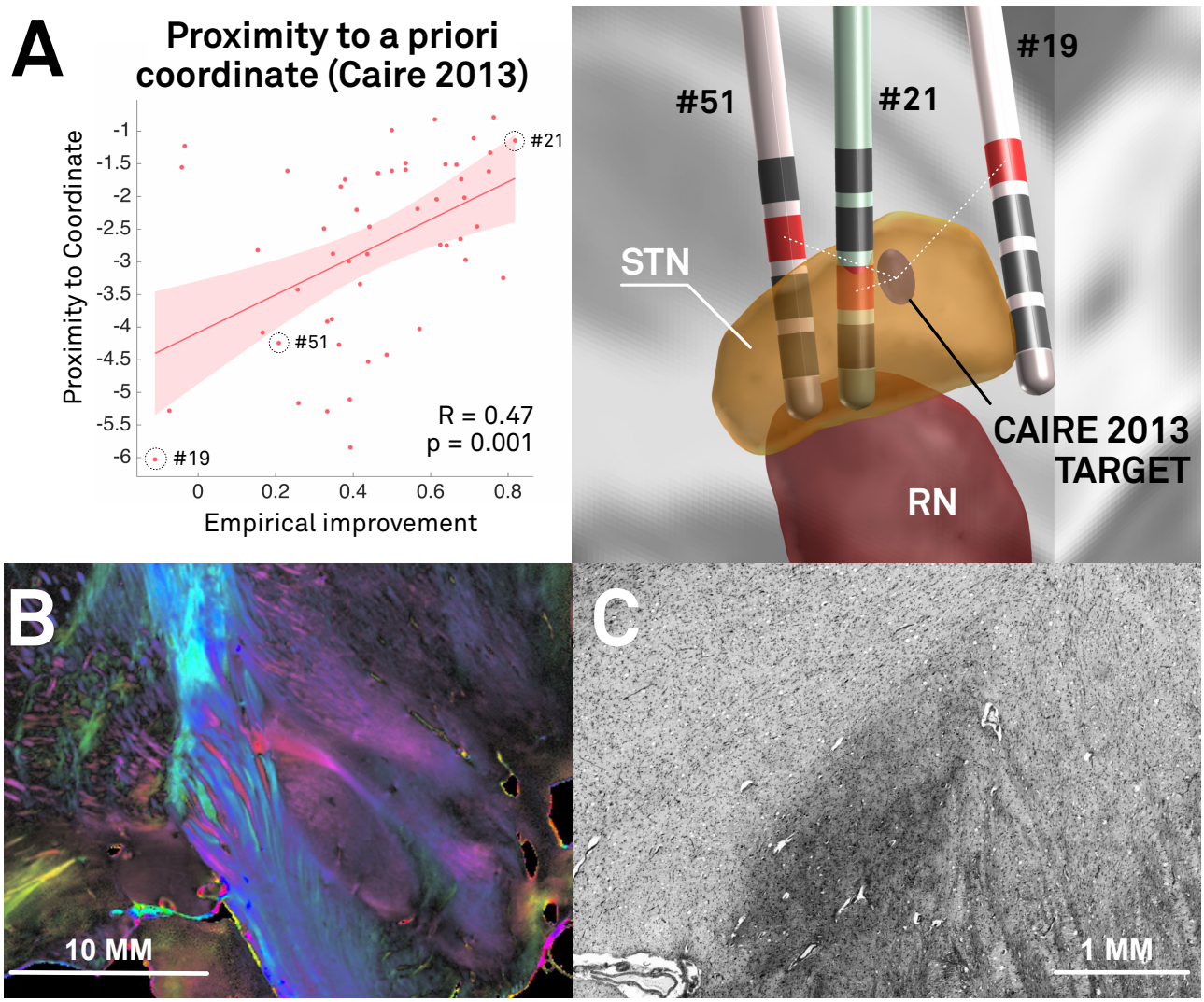

Figure 1: In DBS imaging, "millimeters matter", which poses specific methodological challenges. A) Re-analysis of the Berlin cohort described in (Horn et al., 2017c) shows that proximity of active contact centers to an optimal target is predictive of %-UPDRS-III improvement (left). The target was defined in a meta-analysis (Caire et al., 2013) and transformed to MNI space in a probabilistic fashion (Horn et al., 2017a). Active contacts between electrodes of patients 51 and 21 are a mere two mm away from each other, but result in largely different clinical results (right). The same distance (two mm) corresponds to the average image resolution of functional MRI for which many neuroimaging tools were initially developed. Thus, in the field of DBS imaging, the distance of two mm plays a crucial role, whereas it is often considered insignificant in common neuroimaging studies. B) Coronal polarized light imaging section of the human subthalamic nucleus with surrounding tracts. Image courtesy by Prof. Karl Zilles and Dr. Markus Axer, Forschungszentrum Jülich, INM-1. C) Coronal section of the BigBrain dataset (Amunts et al., 2013) as visualized in the microdraw online application (http://microdraw.pasteur.fr/). Cell sparser and denser subregions are discernible, potentially corresponding to functional zones of the nucleus (Marani et al., 2008). B) and C) demonstrate the tightly-packed anatomical complexity of the STN-DBS target region that is similarly reflected in clinical outcome (A). Of note, only a subregion of this small nucleus is considered an optimal DBS target. The combination of such small and complex DBS targets with a potentially huge impact of small misplacements poses extreme challenges to the field of DBS imaging and raise the need for high-precision pipelines.

Methods

Patient Characteristics, Surgery & Imaging

Example patient

A male patient (65y) suffering from Parkinson‘s Disease received two octopolar segmented DBS leads (Boston Scientific Vercise; BSci, Marlborough, Massachusetts, United States) targeting the subthalamic nucleus (STN). Surgery was done under general anaesthesia with two wakeful phases in which microelectrode recordings were obtained using a Neuro Omega drive (Alpha Omega Engineering, Nazareth, Israel) with a 45° rotated Ben Gun array. In the same session, test stimulations were performed. Recordings started 7.5 mm before reaching the target and were acquired in 15 consecutive steps of 0.5 mm. Recordings of cells with typical STN firing patterns were later transferred to the Lead-DBS session. Test stimulations were made at three mm dorsal to and at the surgical target. In a second surgery five days afterwards, a Boston Scientific Vercise Gevia Impulse Generator was implanted in the chest. Detailed imaging parameters can be found in supplementary material.

Retrospective patient cohort

Data from the patient described above embodies a state-of-the-art example dataset acquired at 3T including a specialized basal ganglia MR sequence and patient-specific diffusion MRI. To further illustrate the impact that different processing streams may have on typical clinical MRI data, we included data from a priorly published retrospective cohort that is described in detail elsewhere (Berlin cohort in Horn et al., 2017c). In brief, 51 patients received quadropolar electrodes (Medtronic type 3389) to the STN region to treat Parkinson‘s Disease. Pre- and postoperative imaging was performed on a 1.5T MRI and included a preoperative T1 and T2 sequence as well as postoperative axial, coronal and sagittal T2 slabs of the basal ganglia. Six of 51 patients received a postoperative CT instead (for detailed imaging parameters see supplementary material and Horn et al., 2017c).

Linear (Within-Patient) Co-Registrations

When a patient folder is loaded in Lead-DBS, a bias-field correction step based on the N4 algorithm is automatically applied to all pre-operative MRI sequences (Tustison et al., 2010). Based on configuration preferences, Lead-DBS chooses one of the preoperative sequences as the anchor modality, i.e. the stationary sequence to which all other

(preoperative and postoperative volumes) sequences are co-registered. By default, the T1-weighted sequence is used or if unavailable the T2-weighted sequence is substituted. This anchor modality is upsampled to isotropic 0.7 mm resolution to maintain high resolution in following steps. This step is common in similar pipelines (e.g. Gunalan et al., 2017). A reason is that (e.g. T2 weighted) acquisitions acquired in clinical routine often come in high in-plane resolution (e.g. 0.5 mm) but poor slice thickness (2-3 mm). If these images are resliced to a 1 mm isotropic MP-RAGE, much in-plane resolution is lost. Thus, our pipeline compromises on a 0.7 mm isotropic working space to which the anchor modality is resliced (images need to be resliced for multispectral normalizations). Several linear registration algorithms are included in Lead-DBS (see table 1). In the present example patient and retrospective cohort, all available preoperative acquisitions (i.e. T2, PD, FGATIR as well as the FA volume derived from the dMRI scan) were co-registered and resliced to the upsampled T1 using SPM 12 (https://www.fil.ion.ucl.ac.uk/spm/software/spm12/). Similarly, the postoperative CT was co-registered using Advanced Normalization Tools (ANTs; http://stnava.github.io/ANTs/). Co-registration results were then manually checked using built-in tools that facilitate visual inspection which may be enhanced by automatic edge detection based wire-frame generation of the anchor modality, and false-color overlays.

Co-registration is a crucial step to achieve precise results since the preoperative data is used to define anatomy and the postoperative to define electrode locations. Thus, imprecise registrations lead to erroneous results in the end. In clinical settings, especially on MRI, postoperative volumes are often slabs (i.e. don‘t cover the whole brain). Accurately registering these to preoperative data is especially challenging for registration algorithms and at times, postoperative data must be registered manually (e.g. using tools as 3D Slicer; www.slicer.org).

Nonlinear (Patient-to-Template) Co-Registrations

To relate electrode placement to anatomy and to make them comparable across patients and centers, it is useful to register individual patient anatomy to a template space. These template spaces often allow the most likely location of anatomical structures to be better defined, and can then be used to project subcortical atlases (table 5) or whole-brain parcellations (table 6) onto regions of interest.

In the original Lead-DBS publication, all registrations between patient and template space were performed in a linear way following the approach introduced by Schönecker and colleagues (Schönecker et al., 2009). This approach was especially developed for DBS

and followed a three-step registration with incremental focus on the subcortical region of interest. In the revised version of Lead-DBS, multiple nonlinear options have been added (table 2). Most of the included approaches were adapted with their parameters tuned for optimal results in the DBS context. Most refinements were performed based on experience in the daily use of the pipeline across multiple institutions. Recently, a study systematically analyzed results of various methods in which over 11,000 nonlinear deformations were solved and compared (Ewert et al., 2018a). Results of this study led to the present default presets implemented in Lead-DBS (figure 2). It is beyond the scope of the present work to describe every modification in each method in detail but the ability to explain clinical improvement using some examples was estimated for the retrospective cohort analyzed here and some details about modifications in regard to subcortical optimization are mentioned in the supplementary material.

Brain Shift Correction

During surgery, air may enter the skull after it is opened. This leads to a nonlinear deformation of the brain in relation to the bone which is called brain shift and typically pushes the forebrain into occipital direction (due to supine position of the patient). Especially when the pneumocephalus is still present during postoperative imaging, it introduces a bias between electrode (postoperative image) placement and anatomical structures on preoperative acquisitions. Whilst brain-shift introduces non-linear transforms, applying non-linear registration techniques to correct this would also deform the electrodes projections and corrupt the corresponding anatomical overlap. To avoid this, our brain-shift correction method uses the threefold linear registration described above (see Schönecker et al., 2009 for validation), which is stored internally and applied to DBS electrode placement afterwards (figure S1).

Electrode Localization

In Lead-DBS, the process of reconstructing electrode placement is divided into an automated ("pre-localization") and a manual ("localization") step. A wide range of electrodes from five manufacturers are readily implemented in Lead-DBS (table 7) and it is straight forward to implement custom models.

<u>Automated pre-Localization</u>

For the pre-localization part, four methods are available:

1. Manual click-and-point tool

2. Integration with 3D Slicer in which fiducial points are placed manually.
3. TRAC / CORE approach (Horn and Kühn, 2015)
4. The PaCER toolbox (https://adhusch.github.io/PaCER/; Husch et al., 2017).

In practice, PaCER usually requires very little to no manual refinement compared to the TRAC/CORE algorithm, but requires a postoperative CT acquisition in contrast to the other methods.

Manual Localization

The user-interface of this crucial processing step was specifically designed to allow for highly precise electrode reconstructions. At all times, the postoperative volume is visualized along planes that are cut orthogonally to the electrode (when moving the lead reconstruction in space, these cuts are updated in real time). A specialized “x-ray mode” can be activated in which the same view is enhanced by averaged stacks of orthogonal slices surrounding the lead. This visualization mode is helpful to reconstruct electrodes in poor resolution acquisitions where partial volume effects may blur or even shift the electrode artifact in space.

Estimating the Local Volume of Tissue Activated

The Volume of Tissue Activated (VTA) is a conceptual volume that is thought to elicit additional action potentials due to the electrical stimulations of axons (McIntyre and Grill, 2002). Much work has been done in this regard and models with increasing sophistication were introduced over the years (e.g. Åström et al., 2014; Butson and McIntyre, 2008; Chaturvedi et al., 2013). In contrast, some more clinically oriented papers aimed at finding fast heuristics to determine the rough extent of the VTA based on the stimulation parameters without actually creating a spatial model (Dembek et al., 2017; Kuncel et al., 2008; Lauro et al., 2015; Mädler and Coenen, 2012). Three such simple heuristic models are included in Lead-DBS (Dembek et al., 2017; Kuncel et al., 2008; Mädler and Coenen, 2012), and a more sophisticated, finite element method based approach was added in 2017 (Horn et al., 2017c; table 3). On a spectrum between simple heuristical and highly sophisticated models, it falls in the middle. This model was briefly described in the aforementioned publication and follows the overall concept described in (Åström et al., 2014). However, a full methods description of the specific model has not been published and can be found in the supplementary material.

Connectivity Estimation

In the revised version of Lead-DBS, several possibilities to estimate structural and functional connectivity exist. These are accessible via the submodules Lead Connectome, Lead Group and Lead Connectome Mapper. Moreover, single-patient connectivity metrics may be visually explored in the general 3D viewer module of the software (ElVis).

Methods may be divided into approaches that utilize *patient-specific* vs. *normative/group-level* resting-state functional MRI (rs-fMRI) or diffusion-weighted imaging based tractography (dMRI). Moreover, they can be subdivided in *voxel-wise / data-driven* or *parcellation-/ROI-based* methods.

Patient Specific Connectivity Estimates

A structural-functional processing pipeline was implemented into the Lead Connectome submodule based on the pipeline described in (Horn, 2015; Horn and Blankenburg, 2016; Horn et al., 2014). For rs-fMRI, the pipeline follows the recommendations given in (Weissenbacher et al., 2009). Briefly, this includes motion-correction (SPM based), detrending, regression of white matter and CSF-signals as well as motion parameters and bandpass-filtering (cutoff-values: 0.009-0.08 Hz) of time series. In dMRI, a Gibbs' ringing removal step (Kellner et al., 2015) is performed before passing the diffusion data into either of four tools subsequently used to estimate a whole-brain tractogram (for a list of fiber-tracking methods implemented in Lead-DBS, see table 4). The Gibbs' tracking algorithm was superior to nine competing algorithms in the 2009 Fiber Cup (Fillard et al., 2011) and was added as the first method. Its successor, a model-free version (Konopleva et al., 2018) of the Mesotracker algorithm (Reisert et al., 2014) was subsequently added to equally investigate mesoscopic properties of fiber tracts and support multi-shell diffusion data. Recently, the Generalized q-Sampling Imaging approach (Yeh et al., 2010) implemented in DSI Studio (http://dsi-studio.labsolver.org/) achieved the highest "valid connection" score in an open competition among 96 methods submitted from 20 different research groups around the world (Maier-Hein et al., 2017). As a result, this method was included into Lead-DBS as well. Finally, a dated simple tensor based deterministic method is also available for debugging or testing purposes.

Normative or population based Connectomes

In the DBS field, large cohorts exist in which patient-specific connectivity data is lacking. In such datasets, a novel technique that combines normative group connectome data with single-patient imaging results may be used. These group connectomes were informed by

large cohorts of subjects or patients (e.g. N = 1000 in case of the Yeo 2011 normative connectome) that were often acquired on specialized MR hardware (such as the human connectome scanner at the Athinoula A. Martinos Center, Boston, MA; Setsompop et al., 2013). The utility of such normative connectomes in a clinical context was first demonstrated by mapping various neurological or psychiatric symptoms to networks influenced by stroke lesions (Boes et al., 2015; Darby et al., 2016; 2017; Fasano et al., 2017; Fischer et al., 2016; Laganiere et al., 2016). Recently, the approach was adapted to the field of DBS in first studies (Horn et al., 2017c; 2017b; 2017a) and, in order, to predict clinical outcome of transcranial magnetic stimulation treatment (Weigand et al., 2017).

A natural limitation of the approach is that the normative connectome data does not account for patient-specific differences in brain connectivity. However, despite its potential shortcomings in individualized connectivity, the use of normative connectomes has a major practical advantage, since larger cohorts of DBS patients with individualized connectivity data are not available and connectivity sequences in DBS patients are difficult to acquire postoperatively. As such, this approach is able to utilize large DBS cohorts collected across different centers, while studies using patient-specific connectivity are based on small cohorts (typically N < 25; e.g. Accolla et al., 2016; Akram et al., 2017; Vanegas Arroyave et al., 2016). Along the same lines, the approach may prove particularly valuable for emerging DBS indications in which only a limited number of patients are implanted world-wide. Thus, the ability to retrospectively analyze such DBS datasets despite the lack of patient-specific connectivity data represents a genuine window into understanding the role of brain connectivity in mediating DBS outcome.

The methods utilizing normative connectomes are implemented in the Lead Connectome Mapper, Lead Group and ElVis tools (figure 2). For an overview of normative connectomes available within Lead-DBS, see table 8.

Explaining variance in clinical outcome within the retrospective 1.5T cohort

DBS-Electrodes of the retrospective cohort were localized using Lead-DBS (see fig. 2) after several normalization and registration strategies were performed. Specifically, preoperative acquisitions were registered into template space using the two default approaches (SPM New Segment and ANTs SyN) identified in (Ewert et al. 2018a). In addition, the ANTs SyN approach without the subcortical refinement step was applied. Finally, a T1-only monospectral approach (FSL FNIRT) was added to compare results with a more typical “standard procedure” used in the neuroimaging field. Electrode localizations (performed in native space) where then registered to template space using the

deformation fields obtained by the various approaches and VTAs were calculated using default parameters in template space. Overlaps between VTAs and the subthalamic nucleus as defined by the DISTAL atlas (Ewert et al. 2018b) were calculated for both hemispheres and summed up. In addition, overlap between the E-field and the STN were calculated in a weighted fashion by multiplying the binary STN image with the non-binary E-Field and summing up voxels. Finally, streamlines were isolated from a priorly published normative connectome based on the Parkinson‘s Progression Marker Inititative (PPMI) data (Marek et al. 2011; Ewert et al. 2018) using the E-Field of the SPM New Segment method as a weighted seed.

These imaging based metrics (VTA-STN overlap, E-Field-STN weighted overlap, weighted streamlines seeding from E-Field connected to SMA) were correlated with empirical % improvement on the Unified Parkinson‘s Disease Rating Scale (UPDRS) III. In a second step, they were fed into general linear models (GLM) that additionally included seven additional clinical covariates of the sample (age, sex, percent improvement in Levodopa response, disease duration until surgery, Levodopa Equivalent Daily Dosage (LEDD) ON and OFF DBS as well as %LEDD reduction by DBS). From these GLMs, root-mean-square error (RSME), R^2-Statistic and p-value of the F-statistic as well as significance predictors are reported.

Methods summary

A list of tools to which interfaces exist or that form a native (preinstalled) part of Lead-DBS is given in table 10. To make deliberate choices regarding which option to choose for each processing step, users require a high methodological level of understanding. To account for this, figure 2 gives an overview of the “default pathway” through Lead-DBS which is further demonstrated in detail in a walkthrough-video available online (http://www.lead-dbs.org/?page_id=192).

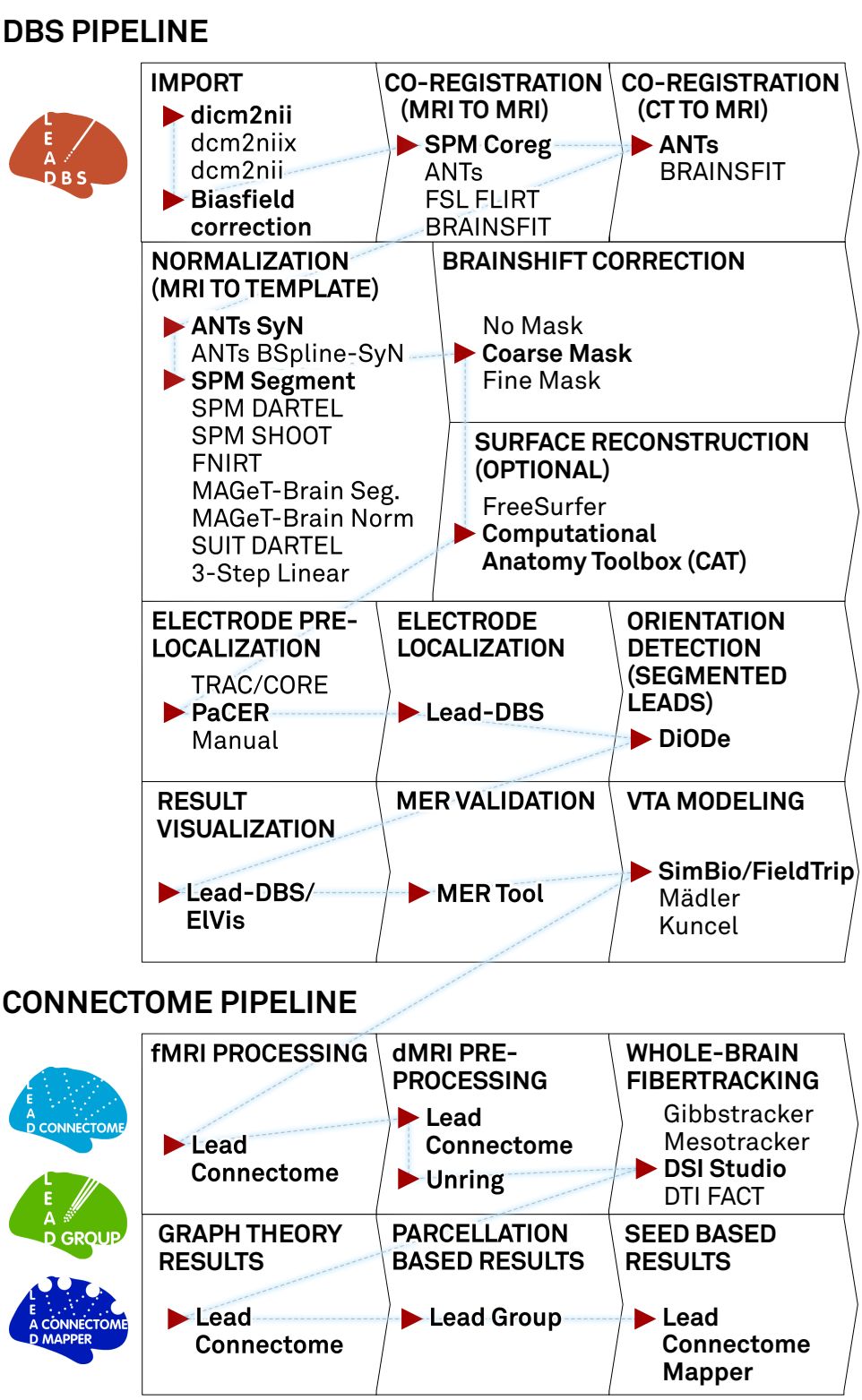

Figure 2: A "default pathway" through Lead-DBS. Processing stages are visualized in consecutive order, general choices are displayed for each step while default selections are marked with red arrow and bold text. For the normalization step, a larger evaluation showed both the ANTs SyN and SPM Segment approaches to perform equally optimal (Ewert et al., 2018a). The DBS and connectome pipelines work in parallel but seamlessly integrate via the order marked by the blue dashed line. After calculating results with Lead Connectome Mapper (last box), results may be used to predict clinical outcome using the Lead Predict tool (not shown) based on a model described in (Horn et al., 2017c).

Results

Patient Outcome

3T example patient: Before surgery, the 64 year male patient had an UPDRS-III score of 64 points (OFF dopamine replacement therapy; Hoehn-Yahr stage IV). Seven days post-surgery, the patient was discharged with an appreciable stun effect and a subjective improvement of gait. Stimulation was set to 0.5 mA bilateral on the lower segmented contacts (ring mode). Under stimulation and medication, a UPDRS-III of four points was taken. At the time of writing, no score under dopaminergic withdrawal and under stimulation is available but will be taken during the three-month postoperative visit.

Retrospective 1.5T cohort: The 51 (18 female) patients were 60 ± 7.9 years old at time of surgery and UPRDS-III improved by 45.3 ± 23.0% from a baseline points (postoperative OFF at 12 months) of 38.6 ± 12.9 to 21.1 ± 8.8 (DBS ON, Med OFF at same day). Disease duration at time of surgery was 10.4 ± 3.9 years and LEDD reduction was 52.8% (1072.72 in baseline vs. 484.57 at 12 months post surgery).

Preoperative baseline of the sample had been 32 ± 11 UPRDS-III points in Med OFF vs. 12 ± 5 points in Med ON conditions (53.5 ± 17.2% percent improvement in levodopa response).

Image Registration

Co-registration results of T2- and if available PD- and FGATIR sequences as well as postoperative MR / CT to the anchor-modality (T1) were done using default presets (figure 2) and were accurate upon visual inspection. Results of the 3T example patient are shown in figure 3A. Similarly, fractional anisotropy (FA) computed from the preoperative dMRI acquisition in the 3T example patient was registered to T1. All preoperative sequences (including FA if available) were used for nonlinear registrations to template space in the ANTs-based approaches (shown in rows 1-3 in figure 4 for the 3T example). In these multispectral warps, the T1-scan was mapped to the T1 template, T2 to T2, PD to PD (figure 3B). The FA volume was instead paired with the FMRIB58 FA template (https://fsl.fmrib.ox.ac.uk/fsl/fslwiki/FMRIB58_FA) that had been registered to 2009b space using an MNI-152 6th-gen to 2009b space transform (Horn, 2016). Since no FGATIR-template exists in 2009b space, Lead-DBS automatically paired this scan with an aggregated PCA template (Horn, 2017). The linear three-step registration was included mainly for reproducibility purposes (Schönecker et al., 2009) but equally supports multispectral registrations. In the MAGeT Brain-like approaches (rows 4-5 in figure 4), only T1-, T2- and

PD-weighted acquisitions were used given these sequences were available in the IXI database of age-matched peer-brains (i.e. “templates” in MAGeT nomenclature). SPM-based approaches (rows 6-7 in figure 4) used all preoperative acquisitions except the FA volume. Here, volumes were not paired with a specific template as in the ANTs-based registrations. Instead, tissue priors were used to learn posterior segmentations using voxel intensities across image modalities (Ashburner and Friston, 2005). All methods except the FNIRT and Linear Three-Step registrations were able to precisely segment the STN target region based on manual inspection. Note that the FNIRT method does not support multispectral warps and estimated the warp based on the T1 volume only (on which the STN is not visible). This may explain the mismatch in template vs. subject STN target regions.

Finally, in the 3T example patient, brain shift correction led to a refined registration between postoperative CT and preoperative anchor modality (T1; figure 5). A shift of 0.17 mm to the left, 0.9 mm to anterior and 1.66 mm in dorsal direction was introduced (figure 4). In the present case, not much pneumocephalus was present and the example may rather demonstrate the introduction of higher robustness and precision with an additional subcortical refinement transform. An example of the tool in case of prevalent pneumocephalus may be seen in the methods figure S1.

Electrode Reconstructions

In the 3T example patient, the PaCER method found an optimal solution including location of electrode contacts in a fully automated manner whereas the TRAC/CORE method robustly reconstructed the trajectory but contacts had to be adjusted manually. Final fully automatic PaCER reconstruction is shown in figure 6. In the subsequent step, orientation of the segmented electrode was reconstructed using the Directional Orientation Detection (DiODe) algorithm, an updated version of the approach described in (Sitz et al., 2017). Relative to a marker position pointing strictly to anterior, rotation of the electrodes was corrected by 65° (right lead) and 30° (left lead) clockwise as seen from the tip, respectively. Final MNI coordinates of planning (lowermost) contacts were x = 11.6, y = -16.2, z = -9.1 on the right and x = -12.7, y = -15.1, z = -10.7 mm on the left. Relative to the midcommissural point, in stereotactic coordinates, these corresponded to x = 11.5, y = -4.4, z = -5.9 (right) and x = -12.7, y = -3.9, z = -7.0 mm (left).

Microelectrode Recordings

After electrode reconstruction, classifications (no cell activity, unspecific cell activity, clear STN typic activity pattern) recorded in the 3T patient were mapped to the subcortex and are shown in figure 7 for the right hemisphere. On both sides, boundaries of firing patterns on the top and bottom of the STN corresponded well to the atlas-/imaging-defined STN. For instance, in the left lateral trajectory, no clear STN activity was reported and in agreement to that, the trajectory traverses outside (lateral) to the imaging-defined STN throughout its whole course.

VTA Calculation

Stimulation parameters of 2 mA on the planning contact (ventral segmented level in ring mode) were calculated using the FEM-model and standard vs. frequency adapted conductivity values (figure 8 A, B). Here, the “heuristic” electric-field (E-field) threshold of 0.2 V/mm was used. The E-Field is the first derivative of the voltage distribution across the tissue surrounding the electrode. To demonstrate the possibilities of segmented electrodes, an additional unidirectional setting was calculated (figure 8 C). Finally, to allow for comparison with heuristic VTA models implemented in Lead-DBS, 2 V estimates on a ring electrode (Medtronic model 3389) are shown in figure 8 D, E using the Mädler or Kuncel models, respectively.

Connectivity from VTA to other Brain Regions

Figure 9 A-C show results of the (3T patient‘s) patient-specific Generalized Q-sampling Imaging (GQI) and Gibbs‘-tracking approaches (whole connectome) as well as a Human Connectome Project (HCP) based normative connectome (Horn et al., 2017a; Setsompop et al., 2013). In figure 9 D-F, GQI based fiber tracts running through the VTA defined in figure 8A and C & D are shown. Figure 10 shows connectivity profiles from the VTA defined in figure 8A projected to the cortex using various structural and functional connectomes.

Explaining clinical improvement in retrospective cohort

Results are summarized in table 9. Briefly, volumes of overlap correlated significantly with the empirical clinical outcome (FSL FNIRT: $R = 0.38$ at $p = 0.007$, ANTs SyN without / with subcortical refinement: $R = 0.47$ / 0.49 at $p < 0.001$; SPM New Segment: $R = 0.52$ at $p < 0.001$). Weighted overlaps between E-Field and STN correlated higher with clinical improvement for all normalization methods (FSL FNIRT: $R = 0.46$ at $p < 0.001$, ANTs SyN

without / with subcortical refinement: R = 0.47 / 0.52 at $p < 0.001$ / $< 10^{-4}$, SPM New Segment: R = 0.54 at $p < 10^{-4}$). Mid column of figure 11 summarizes these findings. When adding additional clinical co-variates to a GLM to explain motor improvement (right column in figure 11), RMSE was comparable between methods (~14-16%) but explained variance was 8% higher between best (SPM New Segment with E-Field) vs. worst (FSL FNIRT with binary VTA) methods (table 9).

Panel A of figure 11 shows the FNIRT method (which does not work multispectrally and had only T1 MRIs as input, thus has poor if any information on the STN location) in combination with a binarized VTA. This approach could be seen as a "common neuroimaging" approach since most fMRI studies use T1 weighted images in their normalization step and binarized VTAs are common in the field. Panels B and C show the two multispectral Lead-DBS default pathways identified in (Ewert et al. 2018a) and apply a weighted VTA (E-Field magnitude). Both yield a similar outcome of ~R = 0.5, increasing the amount of variance explained by imaging alone from ~14% (FNIRT T1) to ~26% (Lead-DBS defaults). Their connectivity strength (number of weighted streamlines to the SMA as defined by the 6ma entry – the medial and anterior parcel of sensorimotor numbered results – of the Glasser et al. 2016 parcellation) was calculated using Lead Connectome Mapper. Resulting values were equally correlated with empirical motor improvement scores (fig. 11 panel D).

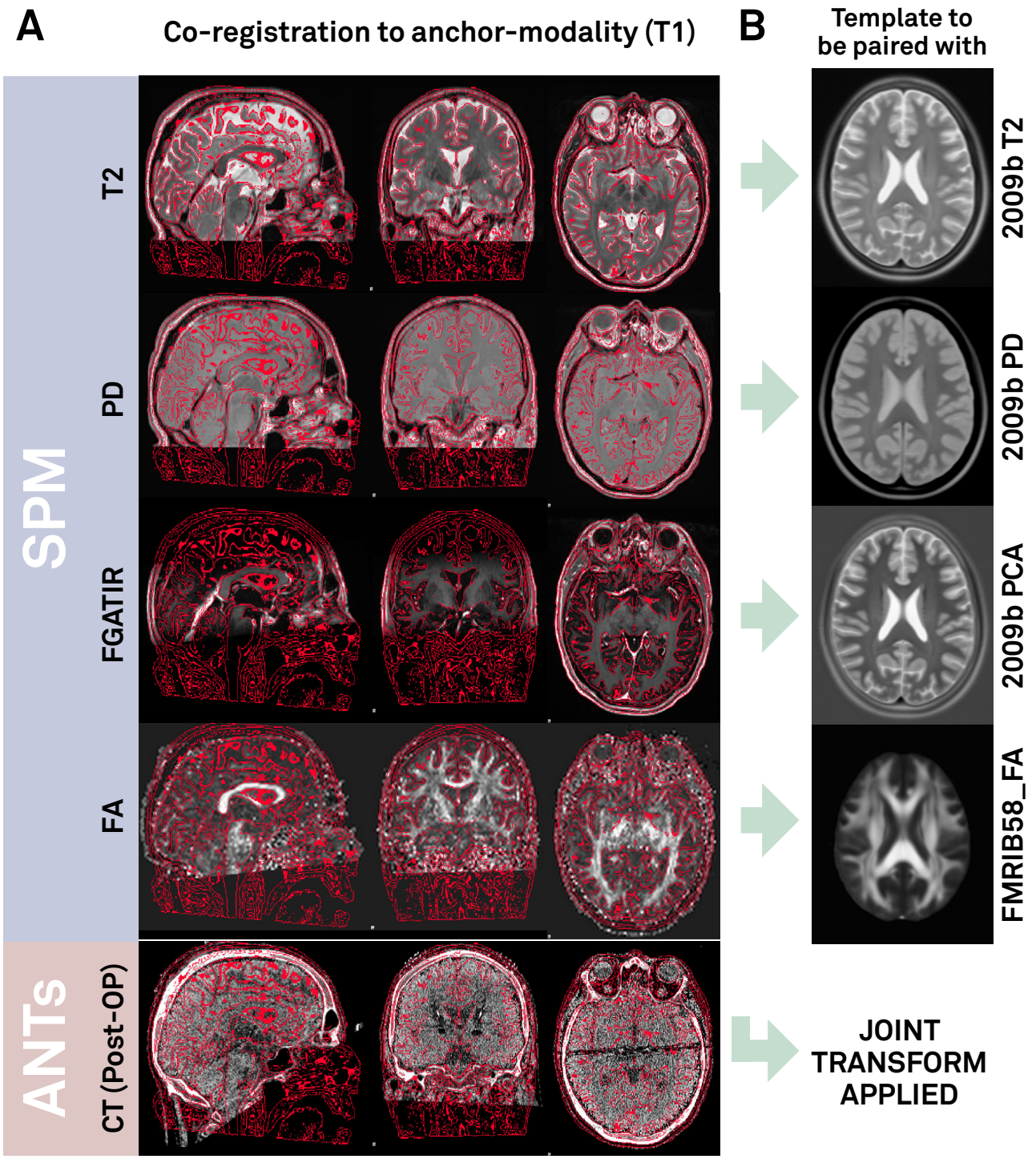

Figure 3: A) Co-registration results of the 3T example patient. Lead-DBS linearly registers preoperative T2, PD, FGATIR and FA volumes to the T1 anchor modality (visualized as red edge contours) using SPM. Similarly, by default, postoperative CT is linearly mapped to T1 using ANTs. A tone mapped version of the CT is shown (equally displaying brain- and bone-windows). B) In the following ANTs-based normalization step, the T1 volume will be registered to the T1-weighted MNI template (2009b NLIN Asym space; not shown). Likewise, T2 and PD volumes will be mapped to T2-/PD-templates. FGATIR volume by default is mapped to a synthetic PCA template while FA to a registered version of the FMRIB58_FA template. These five transforms result in a joint nonlinear deformation field that is equally applied to pre- and postoperative acquisitions.

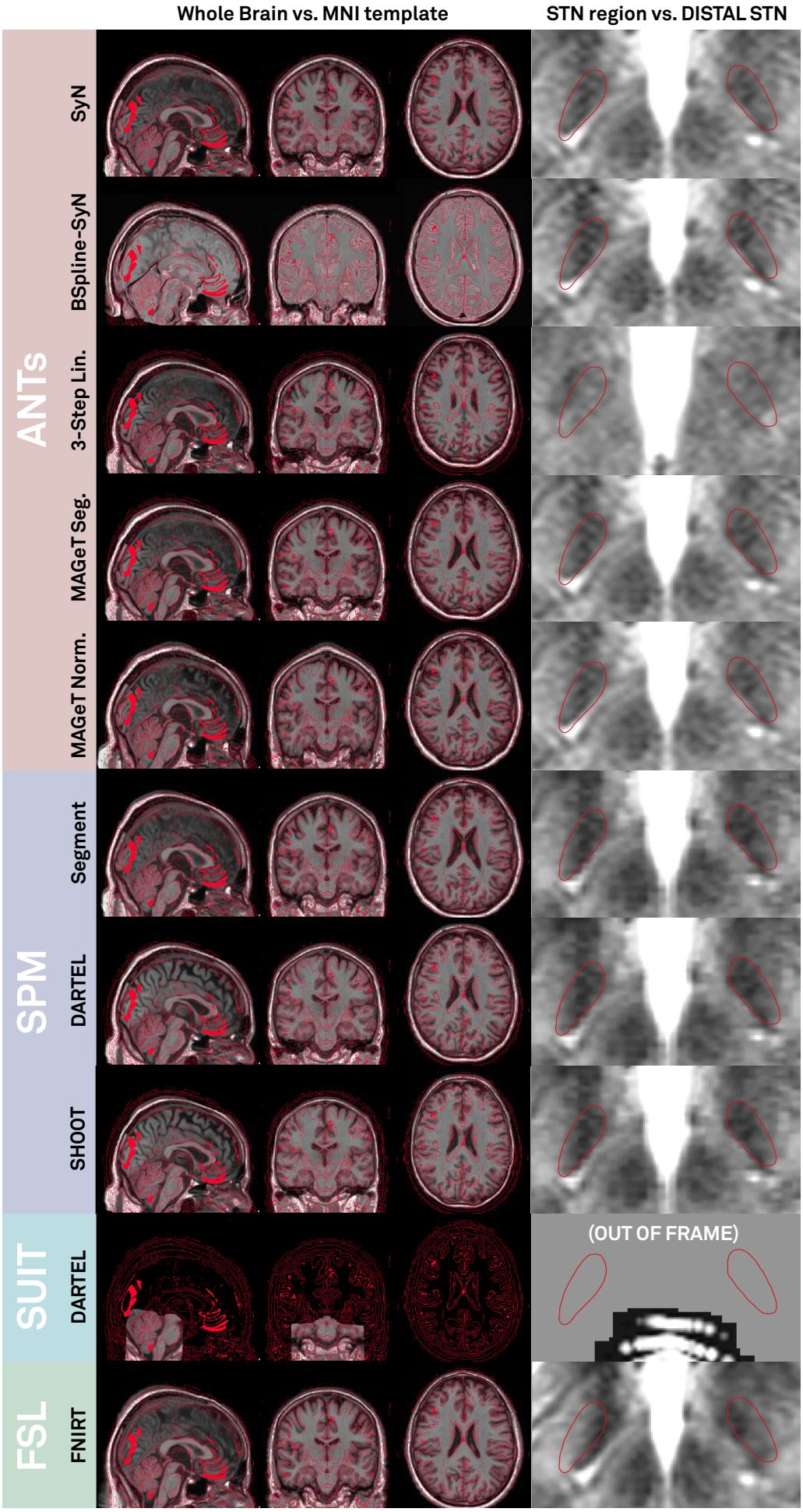

Figure 4: Normalization results of the 3T example patient. Based on the preoperative multimodal MRI (T1, T2, PD, FGATIR) of the patient, individual anatomy was registered into ICBM 2009b NLIN Asym ("MNI") space using various methods. Left column: MNI space (red wireframes) overlaid to normalized T1 acquisition. Right column: DISTAL atlas STN (red wireframes) overlaid to normalized T2 acquisition. Note that the SUIT registration uses SPM methods too, but is based on a toolbox focusing on brainstem and cerebellum anatomy. Thus, normalizing the STN region with this preset is not possible, the method is still displayed for the sake of completeness. It is applicable for brainstem targets such as the Pedunculopontine Nucleus (PPN).

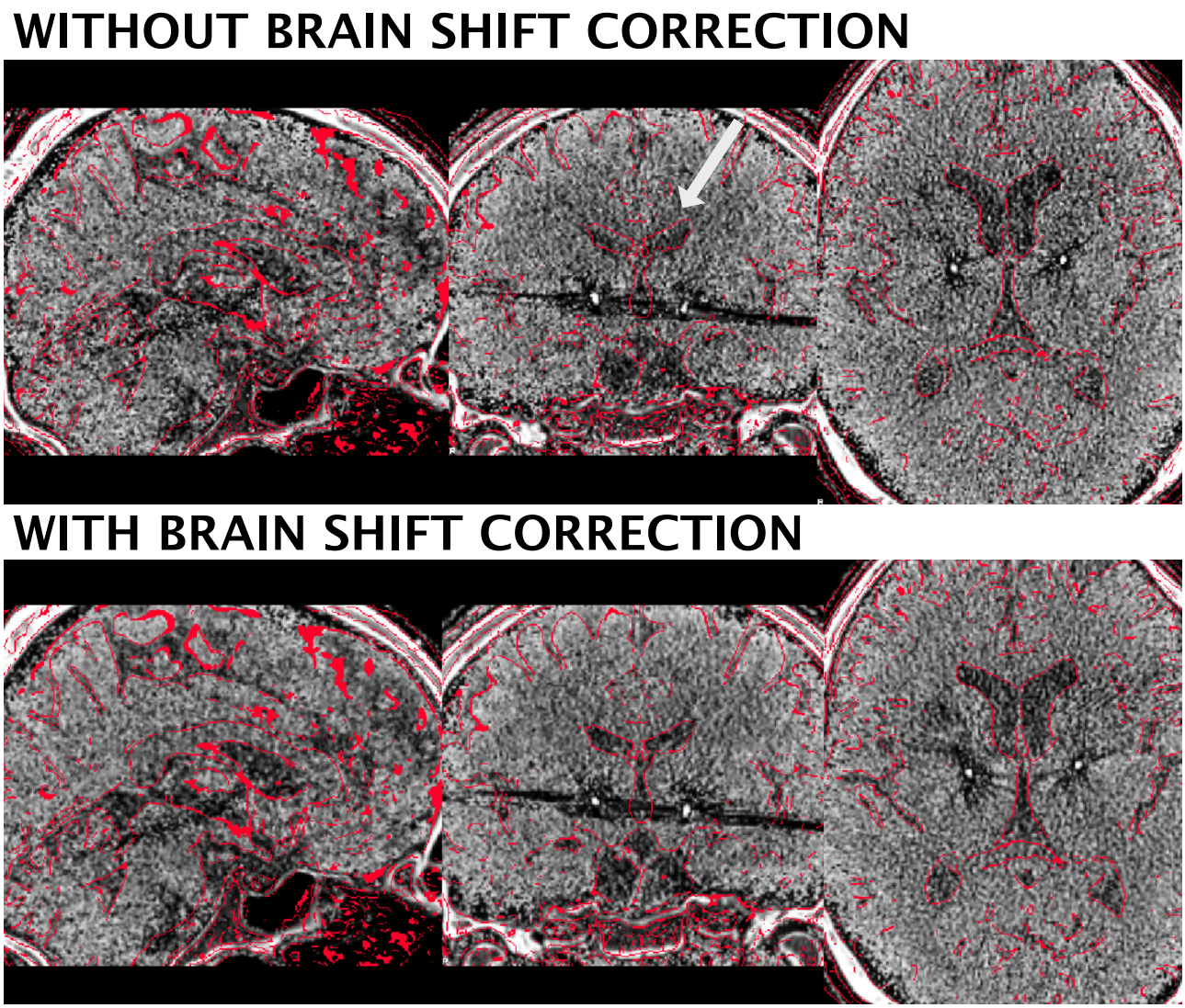

Figure 5: Brain shift correction results of the 3T example patient. The approach serves as a refinement registration step between post- and preoperative acquisitions and is able to minimize nonlinear registration errors due to pneumocephalus (figure S1). In the present example, the postoperative CT was shifted by 1.66 mm in z-, 0.9 mm in y- and 0.17 mm in x-direction. A better registration can best be seen in the area of the ventricles (white arrow). Postoperative CT was tone mapped to show contrast in both brain and skull windows.

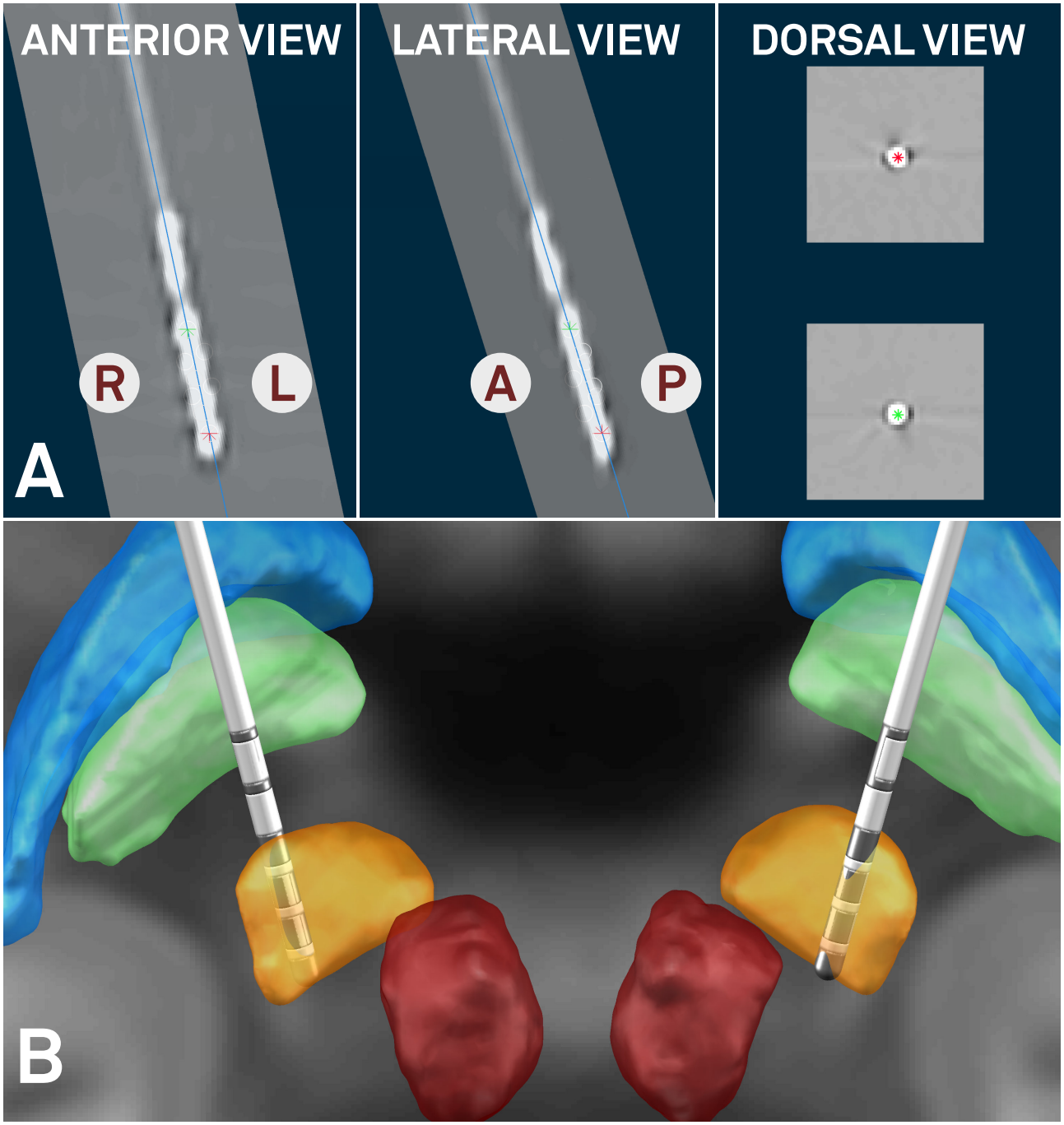

Figure 6: Fully automated electrode reconstruction results (PaCER method contributed by Husch and colleagues) of the 3T example patient. Orientation of lead reconstructed using the method by Sitz and colleagues. A) Postoperative CT is shown orthogonal to reconstructed trajectory (right hemisphere, blue line) in anterior, lateral and dorsal views. Ventral- and dorsalmost contacts marked by red and green asterisks, respectively. Using this view, users can fine-tune electrode reconstructions in a very precise way. B) Final 3D rendering of results in synopsis with key structures defined by the DISTAL atlas. Both electrodes placed in dorsolateral STN which corresponds to the sensorimotor functional zone of the STN. Right lead resides minimally more medial than left (in respect to atlas STN) which can be accounted for by field steering (figure 8).

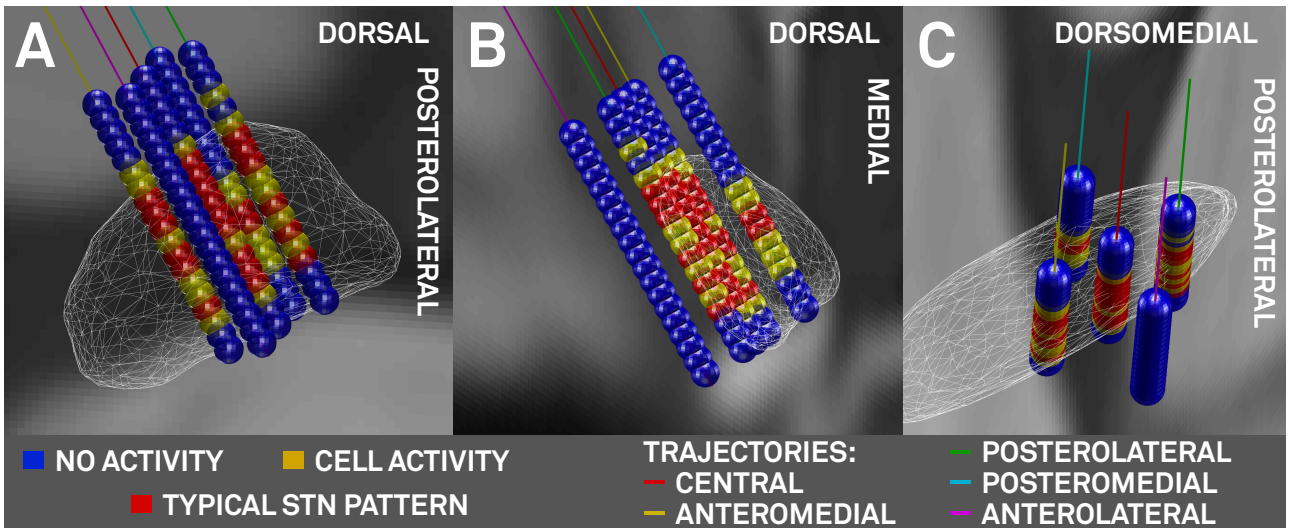

Figure 7: Left-Hemispheric microelectrode recording results of the 3T example patient. A) oblique view orthogonal to the lateral surface of the STN (white wireframes). B) view from posterior and C) dorsal. Markers in blue (no cell activity), yellow (cell activity), red (typical STN firing pattern) placed on 45° rotated Ben Gun (X-) array of microelectrodes between 7.5 and -1.5 mm distance to surgical target in 0.5 mm steps. Trajectories: central (red), lateral (magenta), medial (cyan), posterior (green) and anterior (yellow) trajectories.

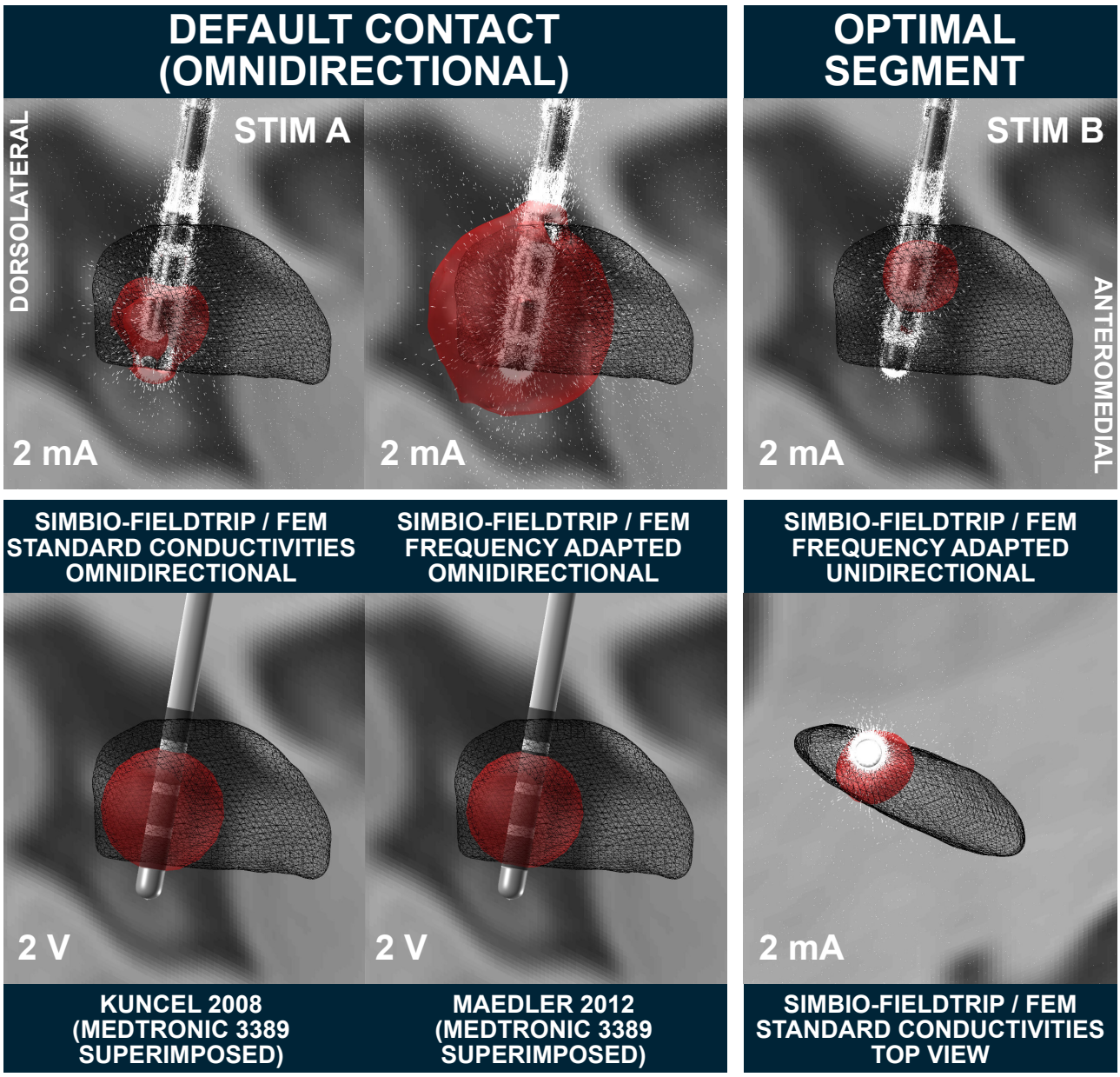

Figure 8: VTA modeling (right hemispheric lead) in the 3T example patient. Left two columns: several omnidirectional stimulations at the default contact. Top row demonstrates the strong impact on standard conductivities vs. frequency-adapted conductivities in the resulting FEM-based VTA. Bottom row shows two heuristic voltage driven models implemented in Lead-DBS. These models are not validated for directional leads, thus, a Medtronic 3389 electrode is visualized instead. Right column: The “optimal” segment on the top (K13) is used as cathode, steering the field anterolaterally to reach a good coverage of the dorsolateral STN. Simulations marked with Stim A and B are used as connectivity seeds in subsequent figures.

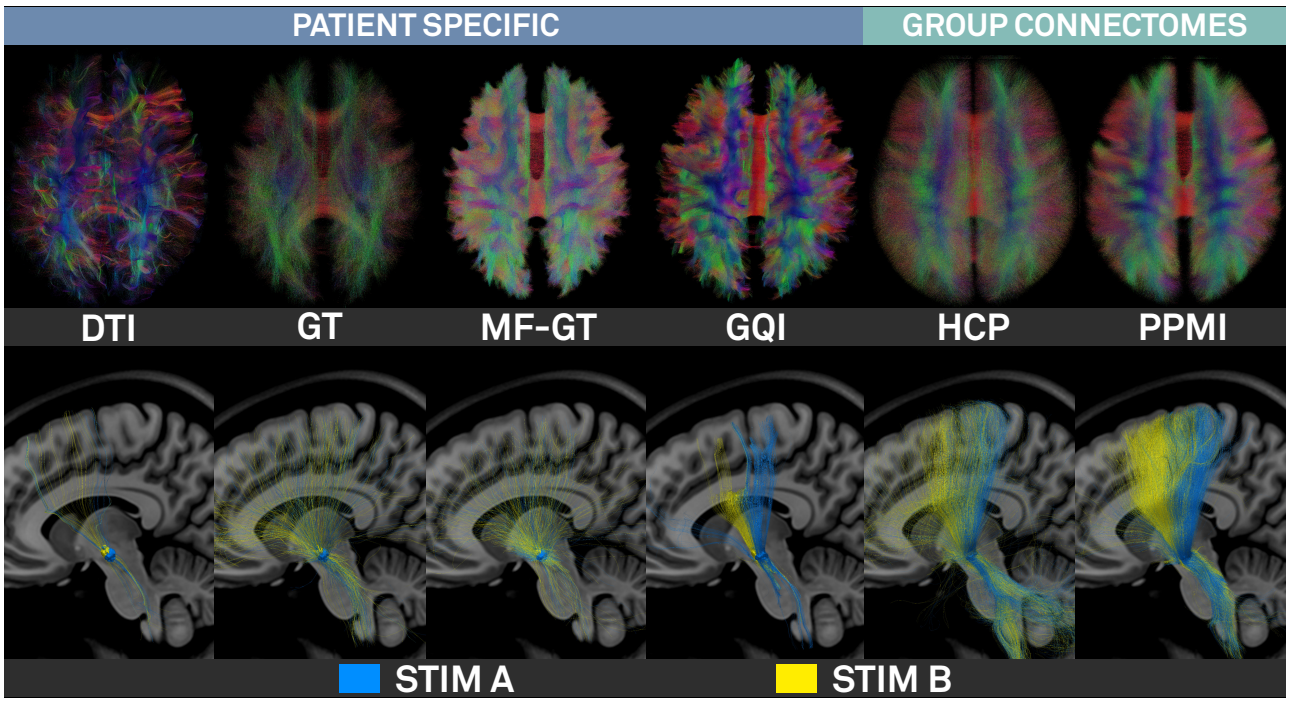

Figure 9: Fiber tracking results of the 3T example patient. First four columns show results of the patient-specific DTI, Gibbs'-tracking, Modelfree Meso global tracker and GQI approaches (top: whole connectome, bottom, tracts seeding from STIM A & B; see figure 8). Last two columns show the same views on HCP and PPMI based normative connectomes.

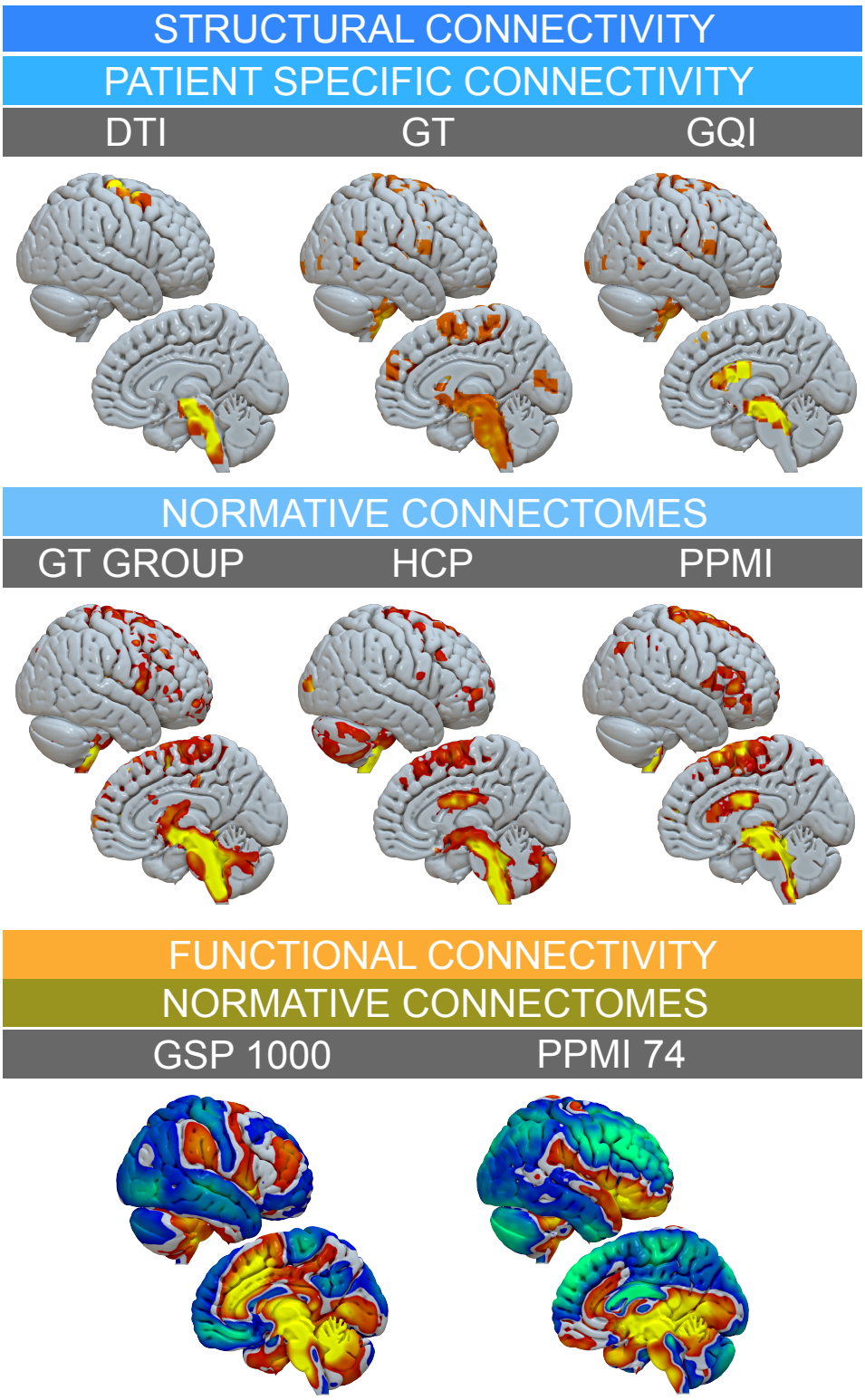

Figure 10: Connectivity from VTA defined by "STIM A" (figure 8) projected on the right hemispheric surface as defined by various connectomes. Top row: Patient specific structural connectivity using DTI, Gibbs' Tracking and GQI methods. Mid row: Connections defined by the structural Gibbsconnectome, HCP Adult Diffusion and PPMI PD connectomes. Bottom row: Functional connectivity between VTA and other brain regions as defined by normative GSP 1000 and PPMI 74 PD connectomes. This figure demonstrates a multitude of options to analyze VTA connectivity in Lead-DBS, but also highlights challenges of the process, since different methods/datasets yield different results.

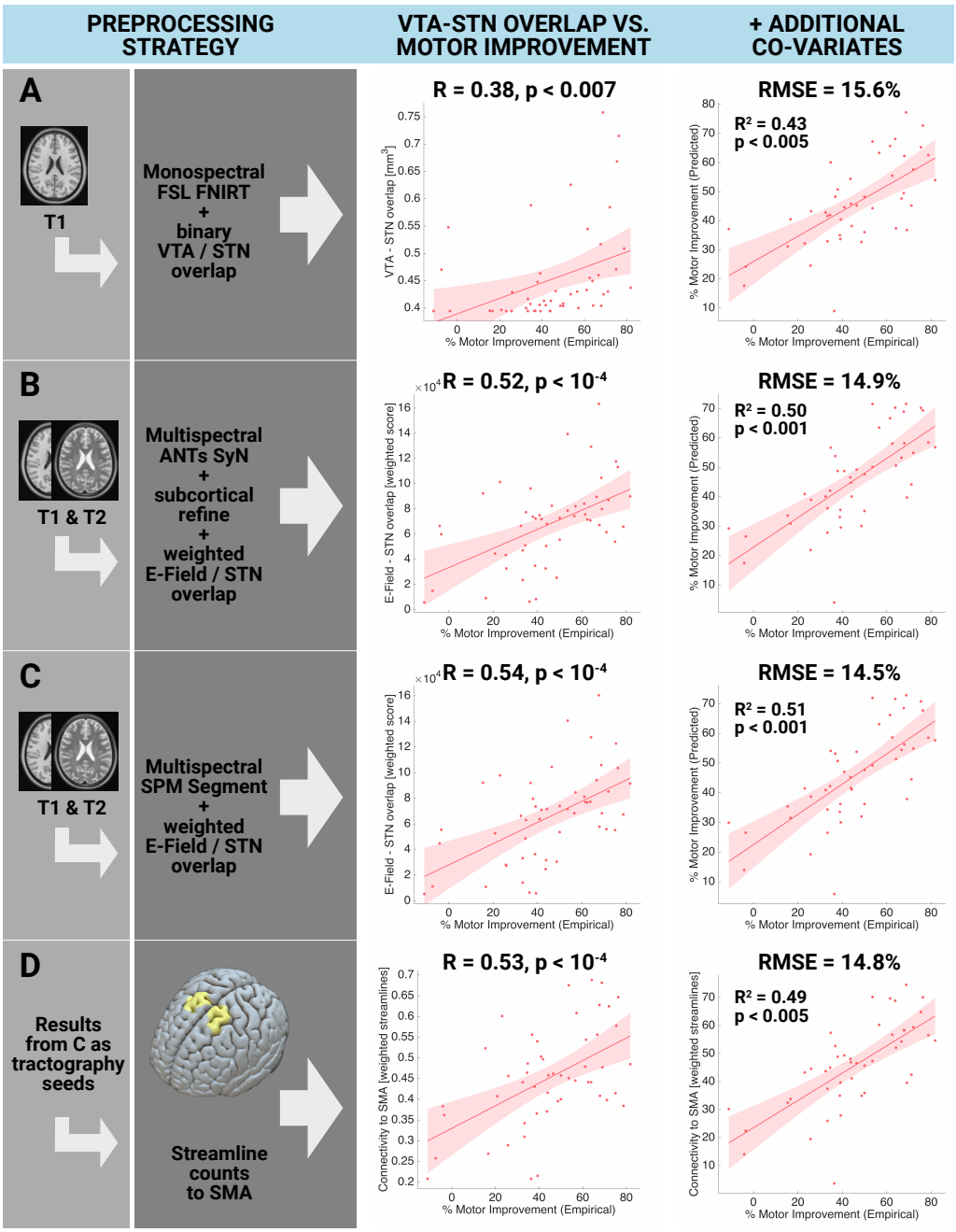

Figure 11: Amount of variance in clinical outcome explained when applying various preprocessing options (retrospective 1.5T cohort). A) an exemplary "standard neuroimaging" approach with a monospectral (T1 only) FSL FNIRT based registration and a binary VTA. B & C) Default pathways of Lead-DBS, registering preoperative data into template space in multispectral fashion according to the most optimal method as delineated in (Ewert et al. 2018a). In these approaches, the overlap sum between the E-Field gradient magnitude inside the STN was calculated. D) Using results from C as weighted seeds to isolate fibers from the normative PPMI connectome (table 8), correlating weighted numbers of streamlines to SMA to explain clinical motor improvement. First column of scatterplots shows direct correlation between VTA-STN overlap (weighted E-field overlap or weighted streamlines to SMA) with clinical improvement. Second column shows GLM with additional clinical covariates. Table 9 shows results for additional preprocessing strategies.

Discussion

We present a comprehensive and advanced processing pipeline to reconstruct, visualize and analyze DBS electrode placement based on neuroimaging data. Specific strengths in comparison to other tools are a seamless integration with a wide array of neuroimaging tools (table 11), a strong focus on precise spatial normalization and connection to a structural and functional connectome pipeline that facilitates connectivity analyses within the DBS context (figs. 9 & 10).

Contributions of the present paper are three-fold. First, an overview is provided regarding the novel neuroimaging methods that were added or updated over the course of four years since the initial publication of Lead-DBS. Second, a default pathway navigating through the multiple options in both DBS and connectome pipelines is outlined (figure 2). This pathway is motivated by both empirical data (Ewert et al., 2018a; Fillard et al., 2011; Klein et al., 2009; Maier-Hein et al., 2017) and by the experience of the Berlin DBS center where Lead-DBS or similar applications were used to localize roughly three thousand DBS electrodes since 2008. Third, results of various processing steps are visualized for a single patient and quantitatively analyzed in a retrospective analysis of 51 patients. In the latter, we do not only demonstrate that overlap between stimulation volumes and the subthalamic nucleus may explain clinical motor improvement, but we also show that the amount of variance explained may depend on the applied preprocessing strategy. Specifically, in the cohort investigated here, the advanced multispectral normalization pipelines implemented as defaults in Lead-DBS are able to explain more variance in clinical outcome than a “typical neuroimaging” pipeline.

In total, Lead-DBS includes five methods for linear co-registrations (table 1), ten normalization approaches (table 3), four approaches for electrode reconstructions, four VTA models (table 4) and four whole-brain tractography pipelines (table 6). Twenty-four subcortical atlases (table 2) and 17 brain parcellations (table 7) are pre-installed. Finally, two functional and four structural connectomes were converted into a format suitable for use in Lead-DBS (table 8). Taken together, these resources build a comprehensive toolbox for DBS electrode localization and the analysis of local (coordinate- or VTA-based) and global (structural and functional connectivity) features. While the number of these methods may introduce complexity, a user-friendly “default pathway” (figure 2) was established which works robustly and well for most applications. This pathway was established while working on several studies that were empowered by Lead-DBS with a variety of clinical

and scientific aims. Some of these used Lead-DBS to integrate population based neural activity with anatomical structures ("Subcortical Electrophysiology Mapping" approach; Accolla et al., 2017; Geng et al., 2018; Horn et al., 2017b; Lofredi et al., 2018; Neumann et al., 2017; van Wijk et al., 2017). Other studies used connectivity profiles from DBS electrodes to predict clinical outcome (Horn et al., 2017c) or combined electrophysiological measures with DBS contact connectivity profiles (Accolla et al., 2016). In an effort to improve the safety profile of DBS implantations, some aimed at determining the relationship between electrode positions and clinical side effects or non-motor symptoms (Mosley et al., 2018b; 2018a). Finally, in other publications, the main aim was to ensure that the analyzed electrodes were indeed placed within the target region (Barow et al., 2014; Brücke et al., 2014; Ehlen et al., 2017; Hohlefeld et al., 2015; 2017; 2013; Krause et al., 2015; 2016; Kroneberg et al., 2017; Merkl et al., 2016; Neumann et al., 2015; 2016; Schroll et al., 2015; Tiedt et al., 2016).

The precision of Lead-DBS

Quantifying the precision of the processing pipeline is a difficult task but a frequently asked question and crucial to the widespread use of the tool. Unfortunately, without postmortem histological examination, no real ground truth exists. However, some indirect measures may help to address the question. First, it should be mentioned that errors may originate from several sources including i) MR-distortion artifacts, ii) within-patient co-registration including brain shift, iii) patient-to-template normalization and iv) electrode localization. Quantifying the first source falls under the domain of MR physics research and goes beyond the present scope. Still, it is advisable to apply distortion correction steps in each MR sequence if possible – even more so when high field magnets are involved. Second, errors in linear co-registration can be minimized by care- and skillful inspection of the data. The check co-registation and brain shift correction modules were specifically designed for the task at hand and iteratively improved to suit the needs and precision of DBS imaging. For instance, the brain shift correction step often sensibly corrects registrations on a submillimeter scale (figs 5 and S1). Normalization procedures were recently addressed in a comparative study (Ewert et al., 2018a). The study defined the default normalization pipeline which, depending on data quality, resulted in an average surface distance of STN/GPi boundaries between 0.38 and 0.75 mm, while inter-rater distance was between 0.41 and 0.82 mm. Based on these results, the pipeline is able to segment STN and GPi nuclei equally well as human experts. In this context, an anteroposterior iron gradient in the STN poses an additional problem for this specific target. The posterolateral sensorimotor part of

the nucleus that is targeted to treat movement disorders contains less iron than its anteriomedial parts, often rendering it smaller on MRI than it actually is (Dormont et al. 2004, Richter et al. 2004, Schäfer et al. 2011, de Hollander et al. 2014, Massey et. al 2012). This makes the registration of this specific nucleus to a template space more error-prone than other targets and yet again raises the need for ultra high-field multispectral preoperative imaging (e.g. see Forstmann et al. 2017, Keuken et al. 2014). Fourth, in the electrode reconstruction step, prior studies have used phantoms to verify that electrode artifact centers in MRI (Pollo et al., 2004; Yelnik et al., 2003) and CT (Hemm et al., 2009; Husch et al., 2017) indeed correspond to electrode centers in the brain. To this end, the PaCER algorithm as the default reconstruction algorithm for postoperative CT yielded an average reconstruction error below 0.2 mm – again depending on data quality. On the other end of the spectrum, the "x-ray mode" of Lead-DBS was specifically designed to reduce errors introduced by partial volume effects in imaging data of suboptimal resolution. In summary, all sources of error can be minimized by using high-quality imaging data, distortion correction and careful inspection or registration and localization results. Based on the retrospective cohort analysed in the present study, we demonstrate that the specialized and elaborate default pipeline of Lead-DBS may add to the amount of variance explained in DBS imaging data.

Reproducibility, Open Science & Experimental Features

As stated above, a key mission of Lead-DBS development is to provide a platform for DBS imaging that is and remains i) free of use, ii) reproducible, open source & transparent, and iii) independent from commercial manufacturers. While this hinders the application in a clinical context (see below), within research, it has several advantages. First, the free software nature offers excellent worldwide accessibility, the possibility of fast skill dissemination in open workshops or courses within the academic field. Similarly, it is easy to script, automate and modify as permitted by the open source license while this is tedious or impossible in closed environments of clinical software. Second, transparent and open source code that is developed in a version controlled fashion (https://github.com/leaddbs/leaddbs) permits excellent reproducibility that is required for good scientific practice. In contrast, undocumented changes or discontinuity in the commercial applications may impose risks for producing consistent results. Discontinuation of commercial products has happened on multiple occasions in the field of DBS (table 10). Consequently, published studies that used discontinued software exist and are now hard if not impossible to reproduce. A slightly less obvious advantage of academic software is that

its development is much more flexible. Commercial applications undergo highly involved and time-consuming certification processes to achieve CE-marks or FDA-approvals for safe use in clinical context. Needless to say, this is a great advantage or even requirement for clinicians but may drastically slow down software development. Furthermore, new research tools may not be easily integrated into commercial pipelines since these would require re-certification. In contrast, new tools can be integrated into academic software from idea and concept to end-user deployment within days. For instance, in 2009, the global fiber tracking approach (Reisert et al., 2011) won the Neurospin Fiber Cup evaluated as the best fiber tracking software compared to nine competitors (Fillard et al., 2011). With help from its developers, the Gibbs‘ Tracker was integrated into the Lead Connectome pipeline within weeks. Recently, a newer comparative study found that the generalized q-sampling algorithm implemented in DSI studio yielded the highest "valid connection" score (Maier-Hein et al., 2017). Again, with kind support and permission of the developer, this method was integrated into Lead-DBS. A last example is the brain shift correction feature that was developed from idea to published code during a three day “brainhack global” event in 2017 at MIT (Craddock et al., 2016). Finally, a strong focus of clinical applications lies on their usability and processing speed. This is important since tools are used by medical personnel working under stressful circumstances where introduction into various complex software tools and long processing times are not tolerable. In contrast, in a research setting, search for innovative application, and development of new features outweighs the burden of computational time. Often, high performance compute clusters are available or jobs are run overnight. Thus, processes with high computational cost will be optimized for speed and standard applications in the former and for development and precision in the latter context. These thoughts illustrate that both types of tools – i.e. clinical vs. academic software – are needed. Given contradictory demands, a one-stop solution serving all purposes is hard if not impossible to create.

Limitations and Future Directions

In comparison to the first release, version 2 represents a major update and a drastically enhanced pipeline for DBS imaging. However, further development is planned to address remaining limitations and further maximize precision of the pipeline. To this end, the pipeline and resulting models may be broken down into four layers, each of which could be further improved as technology and methodology advance (figure 12). First, an anatomy

layer describes the local surroundings of the electrode and helps to define electrode placement initially. This layer is presently defined by imaging and brain atlases (of which some may be informed by histology or other sources of information, table 2). It was mentioned multiple times that naturally, overall precision drastically depends on imaging quality (Ewert et al., 2018a; Husch et al., 2017). Crucially, the MR protocol of the 3T example patient represents a state-of-the art pipeline achievable in typical hospital settings and comprises a specialized basal ganglia sequence (FGATIR; Sudhyadhom et al., 2009). However, the diffusion-MRI acquired here may not be optimally suited to investigate the fine and complex details around DBS targets but was possible to scan within clinical routine. An example of a more optimal scan protocol can be found in (Akram et al., 2017). Moreover, as discussed in our original article (Horn & Kühn 2015), the use of postoperative CT or MRI each has specific advantages (higher signal to noise of the electrode on CT but direct visibility of surrounding anatomical structures on MRI, no radiation). It is hard to tell on empirical grounds which is better but the visibility of structures on the MRI generates a strong argument in favor for postoperative MRI – with the possibility to much more deliberately control for accuracy of post- to pre-co-registration around the target region. Similarly specialized methods like quantitative susceptibility mapping (Wang and Liu, 2015) or the use of ultra-highfield MRI (Forstmann et al., 2017; 2014) are other potential ways of increasing anatomical precision. As figure 1 illustrates, DBS target regions are typically small in size and reside in complex surroundings with a multitude of fiber tracts and functional segregations. Thus, sources above and beyond MRI may be needed to refine definition on the anatomy layer. To this end, techniques like polarized light imaging (Axer et al., 2011) or anisotropic scattering imaging (Shin et al., 2014) as well as the registration of histological stacks into template space (Alho et al., 2017; Amunts et al., 2013; Chakravarty et al., 2006; Ewert et al., 2018b; Forstmann et al., 2016; Jakab et al., 2012; Yelnik et al., 2007) are already applied increasingly.

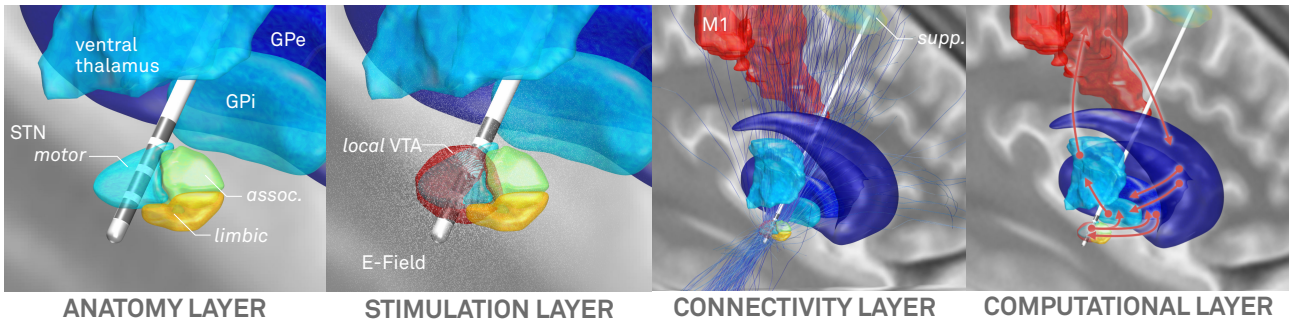

Figure 12: Four layers in a DBS imaging pipeline that may need continuous refinement as technology and methodology advance.

The second layer deals with modeling the local stimulation effects which are often represented by an E-Field or VTA. The anatomy layer directly informs these computations given distinct and even anisotropic conductivity values present in gray or white matter (Butson et al., 2006; Horn et al., 2017c). As mentioned above, to this end, other groups have created much more elaborate models over the last twenty years. Among others, pioneering work by the McIntyre, Butson, Grill, van Rienen and Wårdell groups should be mentioned (e.g. Åström et al., 2014; 2009; Butson et al., 2006; Butson and McIntyre, 2008; Chaturvedi et al., 2013; Gunalan et al., 2017; Schmidt et al., 2013; Schmidt and van Rienen, 2012). A practical disadvantage of these models is that they require manual interventions at multiple stages and use of a multitude of software applications (some of which are expensive commercial solutions; e.g. see Gunalan et al., 2017). On the other end of the spectrum, even simpler models exist that were successfully employed in clinical context (Dembek et al., 2017; Kuncel et al., 2008; Lauro et al., 2015; Mädler and Coenen, 2012; Vanegas Arroyave et al., 2016). Still, while it remains to be shown that more clinical variance may be explained when applying more sophisticated models, the stimulation layer is definitely one where Lead-DBS has yet much room for improvement.

The third layer deals with the transition from a local VTA to a global volume of modulation by applying brain connectivity. Using tractography or functional connectivity to estimate which other brain areas could potentially be modulated by DBS is a powerful technique that was already used to predict clinical outcome in PD patients (Horn et al., 2017c). However, a big challenge is that both methods are highly indirect. As recently demonstrated, tractography results are dominated by false positive connections (Maier-Hein et al., 2017). On the other hand, resting-state functional MRI is only able to give rough statistical dependencies between an indirect measure of brain activity that operates on a very slow temporal scale. Thus, the conclusions drawn from these measures need careful interpretation and benefit from validation via anatomical or electrophysiological work. For instance, the use of combined LFP-MEG recordings (Litvak et al., 2011; Neumann et al., 2015; Oswal et al., 2016) may validate fMRI findings and vice versa, while animal, tracer or gross-dissection studies may be used to interpret tractography results (e.g. Forel, 1877; Iwahori, 1978; T. Kita and H. Kita, 2012; Marburg, 1904). With these limitations in mind, it should be mentioned that the two main tractography algorithms included in Lead-DBS were each best performers in large open competitions (Fillard et al., 2011; Maier-Hein et al., 2017) and a specific advantage of the GQI method in clinical context lies in its low false positive score (Maier-Hein et al., 2017).

Finally, a fourth layer could be seen as modeling dynamics or connectivity changes induced by DBS. This layer is not touched upon here, but computational modeling based on empirical data seems the only way to investigate how brain activity and connectivity responds to stimulation of a specific target. Already, Lead-DBS was used in such basal ganglia modeling studies (Schroll et al., 2015) and an aim of future versions is to incorporate or interface with modeling software – steadily working toward a “virtual patient” model that facilitates a better understanding of DBS.

In conclusion, we present an updated, advanced and integrative platform for DBS imaging research that is openly available with the aim to further elucidate the mechanisms of DBS and improve therapeutic outcome for DBS patients worldwide.

Acknowledgements

This study was supported by Deutsche Forschungsgesellschaft (grants KFO 247, SPP 2041) to AAK, Stiftung Charité, Berlin Institute of Health and Prof. Klaus Thiemann Foundation to AH. TMH has received research support from the American Brain Foundation / American Academy of Neurology and NINDS grant K23NS099380. QF was supported by NIH R01-GM114365 (from NIGMS) and R01-CA204443 (from NCI). TP was supported by the Victorian Government's Operational Infrastructure Support Programme, the Colonial Foundation and the St. Vincent's Hospital Melbourne Research Endowment Fund. JV was supported by the National Science Foundation (NSF): US IGNITE - 10037840. NL, AK, CB, SE, AT, AH, TP, MR, HS, RO, CR, FCY, QF, TMH and JV have nothing to disclose. AAK reports personal fees and non-financial support from Medtronic, personal fees from Boston Scientific and personal fees from St. Jude Medical outside the submitted work. AH and TAD received speaker honoraria from Medtronic outside the submitted work. WJN received travel grants from Medtronic and St. Jude medical outside of the submitted work. Data collection and sharing for this project was provided by the Human Connectome Project (HCP; Principal Investigators: Bruce Rosen, M.D., Ph.D., Arthur W. Toga, Ph.D., Van J. Weeden, MD). HCP funding was provided by the National Institute of Dental and Craniofacial Research (NIDCR), the National Institute of Mental Health (NIMH), and the National Institute of Neurological Disorders and Stroke (NINDS). HCP data are disseminated by the Laboratory of Neuro Imaging at the University of Southern California. The HCP project (Principal Investigators: Bruce Rosen, M.D., Ph.D., Martinos Center at Massachusetts General Hospital; Arthur W. Toga, Ph.D., University of Southern California, Van J. Weeden, MD, Martinos Center at Massachusetts General Hospital) is supported by the National Institute of Dental and Craniofacial Research (NIDCR), the National Institute of Mental Health (NIMH) and the National Institute of Neurological Disorders and Stroke (NINDS). HCP is the result of efforts of co-investigators from the University of Southern California, Martinos Center for Biomedical Imaging at Massachusetts General Hospital (MGH), Washington University, and the University of Minnesota. Data used in the preparation of this article were obtained from the Parkinson's Progression Markers Initiative (PPMI) database (www.ppmi-info.org/data). For up-to-date information on the study, visit www.ppmi-info.org. PPMI - a public-private partnership - is funded by the Michael J. Fox Foundation for Parkinson's Research and funding partners, see www.ppmi-info.org/fundingpartners.

Tables

Table 1: Linear registration methods implemented in Lead-DBS.

Software / Method Name	Used for MR to MR	Used for CT to MR	Publication(s)
ANTs Rigid / Affine	+	+	Ashburner et al. 2007
BRAINSFIT	+	+	Johnson et al. 2007
SPM Co-register	+	–	Friston et al. 2004
FSL FLIRT	+	–	Jenkinson et al. 2002
Hybrid SPM & ANTs, Hybrid SPM & FSL, Hybrid SPM & BRAINSFIT	+	–	*see above*

Table 2: Normalization Methods implemented in Lead-DBS:

Software / Method Name	Adaptations in Lead-DBS	Supports Multispectral Warps	Publication(s)
Statistic Parametric Mapping (SPM)			
Unified Segmentation	Based on Tissue Probability Maps calculated from multispectral ICBM 2009b NLIN ASYM Space templates	+	Ashburner and Friston 2005
DARTEL	Pair-wise instead of group-wise workflow (mapping directly from patient into template space) based on similarly generated DARTEL templates	+	Ashburner et al. 2007
SHOOT	See DARTEL	+	Ashburner and Friston 2011
SUIT based DARTEL	Specialized method if area of interest is in the brainstem (e.g. PPN); Use of SUIT Toolbox based registration to a brainstem/cerebellum template that was registered to ICBM 2009b	+	Diedrichsen et al. 2006, Ashburner et al. 2007
FMRIB Software Library (FSL)			
FNIRT	Standard presets	–	Andersson and Smith 2010
Advanced Normalization Tools (ANTs)			
SyN	Four-Stage preset with subcortical refinement, multiple presets developed for use in DBS	+	Avants et al. 2008
BSpline-SyN	See SyN	+	Tustison & Avants 2013
Other / Specialized			
Linear Three-Step Normalization	Suited for use directly on postoperative MRI (or on preoperative MRI); Implemented using ANTs whereas original code was implemented with use of FSL	+	Schonecker et al. 2009
MAGeT Brain-like Segmentation / Normalization	Multi-Subject/Template implementation inspired by the MAGeT-Brain approach but with strong differences.	+	None / see Chakravarty et al. 2012 for MAGeT-Brain approach
MAGeT Brain-like Normalization	Inversing the idea of MAGeT-Brain by directly averaging deformation fields learned from multiple indirect warps	+	None / see Chakravarty et al. 2012 for MAGeT-Brain approach

Table 3: VTA models included in Lead-DBS.

Method Publication	Type
Horn et al. 2017	FEM Based, 4-Compartment Model, Tetrahedral Mesh
Mädler & Coenen 2012	Heuristic
Kuncel et al. 2008	Heuristic
Dembek et al. 2017	Heuristic

Table 4: Whole-Brain fiber tracking methods implemented in Lead-DBS. Of note, the tensor based method is implemented for debugging purposes and not recommended for actual use.

Tool name	Software	Approach	Support of Single/ Multishell Data	Publication(s)
Gibbs' Tracker	DTI & Fibertools for SPM	Global Tractography	Single-Shell	Kreher et al. 2008, Reisert et al. 2011
Model-Free Mesotracker	DTI & Fibertools for SPM	Mesoscopic Global Tractography	Both	Reisert et al. 2014, Konopleva et al. 2018
Generalized q-Sampling Imaging	DSI Studio	Deterministic Tractography	Both	Yeh et al. 2010
DTI / FACT Tracking	DTI & Fiber Tracking for Matlab	Tensor based Deterministic Tractography	Single-Shell	Dirk-Jan Kroon / Matlab File Exchange

Table 5: Subcortical Atlases suitable for / available within Lead-DBS.

Atlas Name	Pre-installed in Lead-DBS	Source(s) of Information	Structures of Focus / Specialities	Publication(s)
"Made for" Lead-DBS				
DISTAL Atlas	+	Histology, MRI, Tractography	STN, GPi	Ewert et al. 2018, Chakravarty et al. 2006, Chakravarty et al. 2008
Human Motor Thalamus	+	Histology	Motor domains of thalamus, projection from Cb, SN, BG	Ilinsky et al. 2018
Focus on DBS Relevant Structures				
CIT168 Reinforcement Learning Atlas	+	MRI	Based on High Precision MRI	Pauli et al. 2017
ATAG-Atlas	+	MRI	7T MRI based segmentations	Keuken et al. 2014
MNI PD25 Atlas	+	MRI, Histology	Multimodal MR sequences, histology	Xiao et al. 2017, Chakravarty et al. 2008, Chakravarty et al. 2006
Ultra-high Field Atlas for DBS Planning	+	MRI	7T MRI based segmentations	Wang et al. 2016
DBS targets Atlas	+	Literature results	Literature informed DBS targets mapped to MNI space	Horn et al. 2017
BGHAT Atlas	+	MRI	Basal Ganglia Segmentations	Prodoehl et al. 2008
Basal Ganglia Atlas	–	MRI	Basal Ganglia Segmentations	Ahsan et al. 2007
PPN Histological Atlas	+	Histology	Definition of the PPN based on histology	Alho et al. 2017
GPi Probabilistic Parcellation Atlas	+	Tractography	Tractography based parcellation of the GPi	da Silva et al. 2016
Nigral Organization Atlas	+	Tractography, rs-fMRI	Functional zones of substantia nigra segmented by connectivity	Zhang et al. 2017
STN Only				
STN Functional Zones Atlas	+	Tractography	Tractography-based segmentation of STN into functional zones	Accolla et al. 2014
ATAG-Atlas: STN Young–Middle-Aged–Elderly	+	MRI	7T MRI based segmentations, Three age groups	Keuken et al. 2013
Also see DISTAL, Human Motor Thalamus, CIT168, Ultra-High Field DBS, BGHAT & MNI PD25 atlases for definitions of the STN				
Focus on Thalamus				
Morel Atlas	–	Histology	Precise histological atlas of the subcortex	Jakab et al. 2012, Krauth et al. 2010, Morel et al. 2013
Thalamic DBS Connectivity Atlas	+	Tractography	Tractography based parcellation of the thalamus	Akram et al. 2018
Oxford Thalamic Connectivity Atlas	+	Tractography	Tractography based parcellation of the thalamus	Behrens et al. 2003
Thalamic Connectivity Atlas	+	Tractography	Tractography based parcellation of the thalamus	Horn & Blankenburg 2016
Thalamic Connectivity Atlas	+	Tractography, rs-fMRI	Structural-functional connectivity based parcellation of the thalamus	Zhang et al. 2008
Also see DISTAL, Human Motor Thalamus & MNI PD25 atlases for thalamic structures				
Electrophysiological Data				
Electrophysiological Atlas of STN Activity	+	Electrophysiology	Beta Power mapped to STN	Horn et al. 2017

Electrophysiological Atlas of GPi Activity	+	Electrophysiology	Theta Power mapped to GPi	Neumann et al. 2017
Other / Brainstem				
Brainstem Connectome	+	Tractography	Population based fiber tracts of brainstem (HCP data)	Meola et al. 2016
Macroscale Human Connectome Atlas	+	Tractography	Population based fiber tracts of the whole brain (HCP data)	Yeh et al. 2018
BigBrain	–	Histology	Whole-Brain histological stacks registered to MNI space	Amunts et al. 2013
Harvard Ascending Arousal Network Atlas	+	Tractography, MRI	Atlas of Brainstem Structures	Edlow et al. 2012
Whole-Brain Parcellations with subcortical components useful for DBS				
Functional Striatum Parcellation Atlas	+	rs-fMRI	Parcellation of the Striatum into functional zones	Choi et al. 2012
AICHA subcortical regions	+	rs-fMRI	Parcellation of the subcortical structures into functional zones	Joliot et al. 2015
Harvard-Oxford Atlas	+	MRI	Whole-Brain Atlas with subcortical definitions	Frazier et al. 2005
For a list of further whole-brain parcellations, see http://www.lead-dbs.org/?page_id=1004				

Table 6: Brain parcellations (of use for connectomic analyses) suitable for / available within Lead-DBS.

Atlas Name	Pre-installed in Lead-DBS	Source(s) of Information	Structures of Focus / Specialities	Publication(s)
Whole Brain				
Harvard-Oxford cortical/subcortical atlases	+	Manual segmentations	Whole Brain	Makris et al. 2006, Frazier et al. 2005, Desikan et al. 2006, Goldstein et al. 2007
MICCAI 2012 Multi-Atlas Labeling Workshop and Challenge (Neuromorphometrics)	+	Manual segmentations	Whole Brain	neuromorphometrics.com
Brainnetome Atlas parcellation	+	fMRI, dMRI	Whole Brain	Fan et al. 2016
Automated Anatomical Labeling (v2)	+	MRI	Whole Brain	Tzourio-Mazoyer et al. 2002
AICHA: An atlas of intrinsic connectivity of homotopic areas	+	fMRI	Whole Brain	Joliot et al. 2015
Hammers_mith Atlas	+	MRI	Whole Brain, special focus on temporal lobe	Hammers et al. 2003, Gousias et al. 2008
PrAGMATiC	–	fMRI	Functional atlas based on task fMRI	Huth et al. 2016, Huth et al. 2015
fMRI-based random parcellations	+	fMRI	Fine-grained random parcellations informed by rs-fMRI data	Craddock et al. 2012
Voxelwise parcellations	+	MRI	Whole Brain	Horn & Kühn 2015
Cortex Focus				
Mindboggle 101	+	Manual segmentations	Cortex / Desikan protocol	Klein et al. 2012
Yeo functional parcellations	+	fMRI	Cortex	Yeo et al. 2011
Local-Global Parcellation of the Human Cerebral Cortex	+	fMRI	Cortex, refining Yeo 2011 parcellations	Schaefer et al. 2017
Cortical Area Parcellation from Resting-State Correlations	+	rs-fMRI	Cortex	Gordon et al. 2016
HCP MMP 1.0	–	Multimodal	Cortex, surface maps	Glasser et al. 2016
Desikan-Killiany Atlas	–	Gyrification related ROI	Cortex, surface maps	Desikan et al. 2006
Destrieux Atlas	–	Gyrification related ROI	Cortex, surface maps	Destrieux et al. 2010, Fischl et al. 2004
MarsAtlas	–	Gyrification related ROI	Cortex, surface maps	Auzias et al. 2016, Auzias et al. 2013
Specific Subregions				
JuBrain / Juelich histological atlas	+	Histology	Specific regions	Zilles et al. 2010, Amunts et al. 2007, Eickhoff et al. 2005, Eickhoff et al. 2010, Eickhoff et al. 2006bp
Human Motor Area Template	+	fMRI / Metaanalysis	(Pre-) motor cortex	Mayka et al. 2006
Sensorimotor Area Tract Template	+	dMRI	Corticospinal tract subregions	Archer et al. 2017
SUIT cerebellar parcellation	+	MRI	Cerebellum	Diedrichsen et al. 2006, Diedrichsen et al. 2011
Buckner functional cerebellar parcellation	+	fMRI	Same networks as in Yeo 2011 cortical parcellations defined in cerebellum	Buckner et al. 2011

Table 7: Electrode models included in Lead-DBS.

Manufacturer	Type	# Contacts	Contact Spacing	Omnidirectional/ Segmented
DBS				
Medtronic	3389	4	2 mm	O
	3387	4	3 mm	O
	3391	4	7 mm	O
Boston Scientific	Vercise	8	2 mm	O
	Vercise Directed	8	2 mm / Segmented	S
Abbott / St. Jude Medical	Active Tip 6146-6149	4	2 mm	O
	Active Tip 6142-6145	4	3 mm	O
	Infinity Directed 6172	8	2 mm / Segmented	S
	Infinity Directed 6173	8	2 mm / Segmented	S
PINS Medical	L301	4	2 mm	O
	L302	4	3 mm	O
	L303	4	6 mm	O
iEEG				
SDE	08 S8	8	3.5 mm	O
	08 S10	10	3.5 mm	O
	08 S12	12	3.5 mm	O
	08 S16	16	3.5 mm	O

Table 8: Normative Connectomes available in Lead-DBS format.

Name	Repository	N	Population	Publication – Dataset	Processing Methods	Publication – Processing
rs-fMRI based "functional cor						
Functional group connectome 1000 healthy subjects GSP	Harvard Genomic Superstruct Project (GSP)	1000	Controls	Yeo et al. 2011	Lead Connectome fMRI pipeline	Horn et al. 2017
Functional group connectome 74 PPMI PD-patients, 15 controls	Parkinson's Disease Progression Marker Initiative (PPMI)	74 / 15	PD patients, controls	Marek et al. 2011	Lead Connectome fMRI pipeline	Horn et al. 2017
dMRI based "structural conne						
Structural group connectome 20 subjects Gibbs-tracker	Horn 2014 study	20	Controls	Horn et al. 2014	Lead Connectome, Gibbs' tracker	Horn et al. 2014
Structural group connectome 169 NKI subjects Gibbs-tracker	Horn 2016 study	169	Controls	Horn et al. 2016	Lead Connectome, Gibbs' tracker	Horn et al. 2016
Structural group connectome 32 Adult Diffusion HCP subjects GQI	HCP MGH Adult Diffusion dataset	30	Controls	Setsompop et al. 2013	Lead Connectome, DSI Studio (GQI)	Horn et al. 2017
Structural group connectome 90 PPMNI PD-patients GQI	Parkinson's Disease Progression Marker Initiative (PPMI)	90	PD patients	Marek et al. 2011	Lead Connectome, DSI Studio (GQI)	Ewert et al. 2018

Table 9: Preprocessing strategies used to explain variance in 1.5T retrospective cohort.

VTA strategy		**MR volumes used**	**Shown in fig. 11**	**Correlation (image metric vs. motor improvement)**		**GLM (+ additional covariates)**			
Normalization strategy				**R**	**p**	**RSME [%I**	**R^2**	**Overall p**	**Significant predictors ($p < 0.05$)**
Binary VTA overlap									
Monospectral FSL FNIRT		T1	Panel A	0.38	< 0.007	15.1	0.43	< 0.005	Sex
Multispectral ANTs SyN	*w/o subcortical refine*	T1 & T2	–	0.46	< 0.001	15.3	0.45	< 0.005	Sex
	with subcortical refine	T1 & T2	–	0.49	< 0.001	14.8	0.48	< 0.005	Sex, VTA overlap
Multispectral SPM New Segment		T1 & T2	–	0.51	$< 10^{-4}$	14.7	0.49	< 0.001	Sex, VTA overlap
Weighted E-field VTA / STN overlap									
Monospectral FSL FNIRT		T1	–	0.46	< 0.001	15.1	0.46	< 0.005	Sex
Multispectral ANTs SyN	*w/o subcortical refine*	T1 & T2	–	0.47	< 0.001	15.3	0.46	< 0.005	Sex
	with subcortical refine	T1 & T2	Panel B	0.52	$< 10^{-4}$	14.9	0.48	< 0.005	Sex, E-Field overlap
Multispectral SPM New Segment		T1 & T2	Panel C	0.54	$< 10^{-4}$	14.5	0.51	< 0.001	Sex, E-Field overlap
Weighted streamline counts to SMA									
Weighted streamline counts to SMA seeding from E-Field (based method one row above)		T1 & T2	Panel D	0.53	$< 10^{-4}$	14.8	0.49	< 0.005	Sex, Streamlines to SMA

Table 10: Interfaces between Lead-DBS and other neuroimaging tools. Except for FreeSurfer, all tools are available on Windows, macOS and Linux. Necessary binaries for FSL tools were adapted to work on Windows although there is no official Windows FSL release.

Tool Name	Tool Website	Tool Task	Type of Interface	Main Tool Publication
Statistic Parametric Mapping (SPM)	http://www.fil.ion.ucl.ac.uk/spm/software/spm12/	Image Registration & Manipulation	Dependency (Matlab Path)	Friston et al. 2004
FMRIB Software Library (FSL)	https://fsl.fmrib.ox.ac.uk/	Image Registration	Necessary tools included	Woolrich et al. 2009
Advanced Normalization Tools (ANTs)	http://stnava.github.io/ANTs/	Image Registration	Included	Avants et al. 2008
3D Slicer	https://www.slicer.org/	Image Visualization	Dependency, direct uplink via Python calls (System Path)	Fedorov et al. 2012
SurfIce	https://www.nitrc.org/projects/surfice/	Surface Visualization	Included	–
BRAINSFit	https://www.nitrc.org/projects/multimodereg/	Image Registration	Included	Johnson et al. 2007
FieldTrip	http://www.fieldtriptoolbox.org/	Mesh Generation	Necessary tools adapted / included	Oostenveld et al. 2010
SimBio	https://www.mrt.uni-jena.de/simbio/	FEM Modeling	Necessary tools adapted / included	Vorwerk et al. 2018
SUIT	http://www.diedrichsenlab.org/imaging/suit.htm	Specialized Registration (Brainstem)	Dependency (Matlab Path)	Diedrichsen et al. 2006
FreeSurfer	https://surfer.nmr.mgh.harvard.edu/	Surface Reconstruction (ECoG Electrodes)	Dependency (system calls)	Dale et al. 1999
Computational Anatomy Toolbox (CAT)	http://www.neuro.uni-jena.de/cat/	Surface Reconstruction (ECoG Electrodes)	Dependency (Matlab Path)	Gaser and Dahnke 2016
PaCER	https://adhusch.github.io/PaCER/	Electrode Localization	Included	Husch et al. 2017
dcm2nii, dcm2niix, dicm2nii	https://www.nitrc.org/projects/dcm2nii/	DICOM import	Included	Li et al. 2016
Gibbs' Tracker	https://www.uniklinik-freiburg.de/mr-en/research-groups/diffperf/fibertools.html	Fiber tracking	Included	Reisert et al. 2011
Model-Free Mesotracker	https://bitbucket.org/reisert/mesoft_v1	Fiber tracking	Included	Konopleva et al. 2018
DSI Studio	http://dsi-studio.labsolver.org	Fiber tracking	Included	Yeh et al. 2010
Gibbs' Ringing Artifact Removal Tool	https://bitbucket.org/reisert/unring	dMRI preprocessing	Included	Kellner et al. 2015
Network Based Statistics (NBS)	https://sites.google.com/site/bctnet/comparison/nbs	Graph-Theory Level Statistics	Included	Zalesky et al. 2010

Table 11: Software with aims comparable to Lead-DBS. Entries based on publicly available information at the time of writing.

Name	Institution / Company	Publicly available	Open Source	Free of cost	CE / FDA	Website	Citation
Scientific Applications							
DBSproc	NIH	+	+	+	–	afni.nimh.nih.gov	Lauro et al. 2015
PyDBS	Univ. Rennes, Univ. Descartes Paris	–			–	acoustic.univ-rennes1.fr/doku.php/software	D'Albis et al. 2014
PaCER	Université du Luxembourg	+	+	+	–	adhusch.github.io/PaCER	Husch et al. 2017
DBSmapping	INESC TEC Porto	–	N/A	N/A	–	–	Da Silva et al. 2015
"Virtual Patient"	MGH / HMS	–	N/A	N/A	–	–	Bonmassar et al. 2014
CiceroneDBS	Case Western Reserve University	*discont.*	N/A	N/A	–	–	Miocinovic et al. 2007
Lead-DBS	Charité – University Medicine Berlin	+	+	+	–	lead-dbs.org	Horn and Kühn 2015
Commercial Applications							
GUIDE	Boston Scientific	*discont.*	N/A	N/A	N/A	–	N/A
GUIDE XT	Brainlab / Boston Scientific	+	–	–	*filed*	brainlab.com	N/A
Optivize	Medtronic	*discont.*	N/A	N/A	N/A	medtonic.com	N/A
SureTune	Sapiens Steering Brain Stimulation	*discont.*	N/A	N/A	N/A	–	N/A
SureTune vs. 2 & 3	Medtronic	+	–	–	+	medtonic.com	N/A
CranialCloud / CranialDrive	Neurotargeting LLC	+	–	–	+	app.cranialdrive.com	

Supplementary Material

Imaging parameters of the 3T example patient

Presurgical imaging was performed on a 3T MRI system (Skyra Magnetom, Siemens, Erlangen, Germany). The patient was not sedated for imaging. For better visualization of vascular structures, a standard dose of 0.1 mmol/kg gadobutrol was administered intravenously at the start of the procedure. The MRI protocol consisted of the following sequences: head scout (14 s), sagittal 3D T1-weighted gradient-echo sequence (MPRAGE; TR/TE/TI 2300/2.32/900 ms, voxel size 0.9 × 0.9 × 0.9 mm^3, FOV 240 × 240 mm^2; 5 min. 21 s), axial T2 TSE (TR/TE 13320/101 ms, voxel size 0.7 × 0.7 × 2.0 mm^3, FOV 250 × 250 mm^2; 3 min. 48 s), sagittal Fast Grey Matter Acquisition T1 Inversion Recovery (FGATIR; TR/TE/TI 1500/3.56/559 ms, voxel size 0.8 × 0.8 × 1.0 mm^3, FOV 240 × 240 mm^2; 6 min. 17 s), axial proton-weighted TSE (TR/TE 3600/11 ms, voxel size 1.0 × 1.0 × 2.0 mm^3, FOV 250 × 250 mm^2; 3 min. 34 s), and dMRI (EPI, TR/TE 7500/95 ms, voxel size 2.0 × 2.0 × 2.0 mm^3, FOV 250 × 250 mm^2, 20 diffusion-encoding directions with b-value 1000 s/mm^2 and one non-diffusion-weighted b_0-volume; 5 min. 47 s). Overall acquisition time was 25 min. A routine head CT was done the day after electrode implantation using an 80-multislice Toshiba Aquilion PRIME (Canon Medical Systems, Otawara, Japan). Four sequential blocks, each with a length of 37.75 mm, were acquired (280 mA, 120 kV, rotation time 1 s, matrix 512 x 512 mm^2, $CTDI_{vol}$ 55.79 mGy), resulting in a slice thickness of 0.5 mm.

Imaging parameters of the retrospective 1.5T cohort

All patients underwent pre-operative MR-imaging on a 1.5 T scanner (NT Intera; Philips Medical Systems, Best, The Netherlands) using a T2-weighted fast spin-echo (FSE) with the following parameters: TR = 3500 ms, TE = 138 ms, echo-train length: 8, excitations: 3, flip angle: 90°, section thickness: 2 mm, section gap: 0.2 mm, FOV: 260 mm (in-plane resolution 0.51 × 0.51 mm), matrix size: 384 interpolated to 512, total acquisition time, 10 min and 41 s.

Postoperative MR-imaging was performed in 45 patients. DBS patients are subject to a limitation of the specific absorption rate (SAR, b0.1 W/kg), which has been specified by the manufacturer of the electrodes. Within 5 days after implantation of the electrodes, MR-imaging was performed on the same scanner using a T2-weighted fast spin-echo (FSE) sequence in low SAR mode with the same parameters as used pre-operatively. Philips

software Version 11.1 level 4 was used. MR sections in the axial and coronal planes were obtained and processed in this study. In the following, “axial” and “coronal” volumes refer to acquisitions with voxel sizes of 0.51 × 0.51 mm in the axial or coronal planes respectively, each with a 2 mm slice thickness. Postoperative CT was conducted in 6 patients (8 of whom also had postoperative MRI). Here, high-resolution images were acquired on a LightSpeed16 (GE Medical System, Milwaukee, Wisconsin) Slice CT with a spatial resolution of 0.49 × 0.49 × 0.67 mm^3. Images were acquired in axial (i.e. sequential/incremental) order at 140 kV and automated mA setting. Noise index was 7.0. A large SFOV with 50 cm diameter was used.

Methodological details for normalization strategies as implemented in Lead-DBS

SPM Unified Segmentation

In Lead-DBS, the Unified Segmentation approach does not fit warps to the standard tissue probability maps (TPM) supplied with SPM software which are based on a population differing from the original MNI-152 population (IXI-Dataset; http://brain-development.org/ixi-dataset/). Instead, the multispectral (T1-, T2-, PD-weighted) MNI-152 / ICBM 2009b Nonlinear Asymmetric template series were preprocessed using the Unified Segmentation approach, generating a new set of templates. Moreover, this was done using refined tissue priors that include subcortical structures and have been proposed for use in the DBS context (Lorio et al., 2016). This procedure ensures direct compatibility with the 2009b space (Fonov et al., 2009) and the use of these adapted TPM yielded slightly better segmentations of STN and GPi in a recent comparison (Ewert et al., 2018a). Of note, all implementations of SPM methods (Unified Segmentation, DARTEL & SHOOT, see below) within Lead-DBS by default operate on all preoperative acquisitions simultaneously (multispectral normalization).

SPM DARTEL & SHOOT

SPM DARTEL/SHOOT create population-specific group average templates based on the data available (Ashburner, 2007; Ashburner and Friston, 2011). As these are different to MNI space, we adapted the pipeline to register to single subjects directly to MNI space derived from the multispectral 2009b data described above.

Advanced Normalization Tools (ANTs)

ANTs is another non-linear pipeline that has been extensively optimized for LEAD-DBS 2.0 (Ewert et al., 2018a). The current default implementation is a multispectral warp that combines a rigid, an affine and two nonlinear symmetric image normalization (SyN) stages. While the first SyN stage includes the whole brain, the second is limited to a subcortical region mask defined in (Schönecker et al., 2009). The implementation detects and properly handles slabs, which are often used in clinical context. For instance, many centers acquire whole-brain 3D gradient-echo T1-weighted series and a T2-weighted slab of the subcortex for stereotactic planning (Horn et al., 2017c). If slabs are detected, Lead-DBS automatically adds a third intermediate SyN stage that focuses on the area covered by all acquisitions (whereas the linear stages and first SyN stage only takes the whole-brain acquisition(s) into account).

MAGeT Brain-like Segmentation

The MAGeT Brain approach (https://github.com/CobraLab/MAGeTbrain; Chakravarty et al., 2012) was developed for segmentation of deep nuclei and computes multiple warps from atlas space via multiple “templates” to the subject of question. Here, templates refer to additional brains (e.g. high resolution MRIs acquired on specialized hardware). Thus, the deformation from atlas to subject space takes “detours” via multiple different brains and, as a result, multiple solutions for the atlas based segmentation are attained. These solutions are then aggregated (e.g. by simple averaging or majority voting). The intuitive understanding of the approach is that it increases robustness by introducing anatomical variance and the original authors showed this increased precision empirically in multiple studies (Chakravarty et al., 2012; Pipitone et al., 2014).

In Lead-DBS, this concept is adopted and used for both segmentation and normalization. In a first step, key structures defined by the DISTAL atlas in 2009b space (STN, GPi, GPe, RN) are segmented in native space using an adapted MAGeT Brain approach implemented in Lead-DBS using ANTs. In a second step, a SyN-based ANTs-registration from native to template space is computed (see above) that additionally includes the segmented labels as further “spectra” in the warp. For example, if preoperative T1- and T2-weighted acquisitions are present, a six-fold normalization is computed (including T1-patient to T1-MNI, T2-patient to T2-MNI, auto-segmented patient STN to DISTAL atlas STN, patient GPi to DISTAL GPi, etc.). This approach may add additional precision at and around key interest regions in DBS but has not been empirically tested or compared to conventional approaches beyond the original MAGeT publications (Chakravarty et al., 2012; Pipitone et al., 2014).

MAGeT Brain-like Normalization

This further adaptation of the MAGeT Brain approach reverses the idea and directly works on the deformation fields solved during normalization. Specifically, multiple deformation fields warping from subject to template are created, each taking a detour via a peer brain ("template" in the MAGeT-Brain nomenclature). Resulting deformation fields are then aggregated by calculating their voxel-wise robust average. A final deformation field that warps from subject to template space is created that can be applied to warp electrodes into template space. Of note, both MAGeT-inspired methods require the use of "peer-subjects" to include into the analysis. To demonstrate this in the present patient example, 21 age-matched peers from the IXI-dataset (http://brain-development.org/ixi-dataset/) were automatically assigned by Lead-DBS as previously described in similar context (Horn et al., 2017a).

Methodological details for volume of tissue activated generation

Mesh Generation

A cylindrical four-compartment model of the area surrounding the electrode and the lead itself is constructed based on the conducting and insulating parts of the electrodes, gray matter, and white matter. This model is represented by a tetrahedral mesh that is generated using the iso2mesh toolbox (http://iso2mesh.sourceforge.net/) in combination with other meshing tools, including Tetgen (http://wias-berlin.de/software/tetgen/) for the Delaunay tetrahedralization step and Cork (https://github.com/gilbo/cork) for merging electrode and brain surface meshes. We note here that all involved tools are included within Lead-DBS and some interfaces of iso2mesh were slightly modified. The output mesh is truncated by a cylindrical boundary with a radius of 20 mm; a larger radius is automatically used when higher stimulation amplitudes are applied. All regions within the cylinder not covered by either gray matter or the electrode are modeled as isotropic white matter. Gray matter portions are defined by the atlas chosen by the user (table 5). This gray matter model can be either informed by an atlas available in template space, the same atlas that was automatically transferred to native space or a manual segmentation of structures of interest manually performed by the user.

Finally, the conducting and insulating regions are specified by the electrode models supplied with Lead-DBS. A wide range of electrodes from five manufacturers are readily implemented in Lead-DBS (table 7) and it is straight forward to implement custom models. Surface meshes from electrode and atlas as well as the bounding cylinder are resolved to a joint surface mesh using a modified version of Cork as implemented in iso2mesh. This joint mesh is then fed into Tetgen to create a tetrahedral mesh. Tetrahedra within the regions of gray matter, white matter, metal or insulating parts are identified and tagged using a post-processing code implemented in Lead-DBS.

Electric Field Modeling using Finite Element Method (FEM)

Conductivity at each tetrahedron is estimated using the FieldTrip / SimBio pipeline (Oostenveld et al., 2010; Vorwerk et al., 2014; 2018; https://www.mrt.uni-jena.de/simbio/; http://www.fieldtriptoolbox.org/). Conductivity values for gray and white matter can be entered by the user while two presets are available. The first consists of conductivity values commonly used in the field (0.33 and 0.14 S/mm for gray and white matter, respectively). Similar values were used in modeling EEG data (e.g. Buzsáki, 2006; Vorwerk et al., 2014) and in most previous DBS models (e.g. Åström et al., 2014; McIntyre and Grill, 2002). However, these conductivity values are not corrected for stimulation frequency and drop drastically at a typical stimulation frequency of 130 Hz (Hasgall et al., 2015). Thus, a second set of conductivity presets adjusted for stimulation frequency is available (0.0915 and 0.059 S/mm).

Both constant-voltage and constant-current settings can be modeled. The voltage or amplitude applied to the active contacts is introduced as a boundary condition. In case of monopolar stimulation, the surface of the bounding cylinder serves as the anode. Subsequently, the gradient of the potential distribution is calculated by derivation of the FEM solution. Due to the first order FEM approach that is used, the resulting gradient is piecewise continuous. The binary VTA is obtained by thresholding the resulting electric field strength at a user-specified value. In the past, a value of 0.2 V/mm has frequently been used in this context (Åström et al., 2014; 2009; Horn et al., 2017c; Vasques et al., 2009). In Lead-DBS, this value serves as the “general heuristic” default value. Furthermore, based on prior literature, heuristics for STN (0.19 V/mm; Åström et al., 2014; Mädler and Coenen, 2012), GPi (0.2 V/mm; Hemm et al., 2005; Vasques et al., 2009) and Vim (0.165 V/mm; Åström et al., 2014; Kuncel et al., 2008) can be used. Finally, specific activation thresholds that depend on axon diameters (D = 2-5 µm) and stimulation pulse-

widths (t = 30, 60, 90, 120 µs) are available as they were estimated in (Åström et al., 2014).

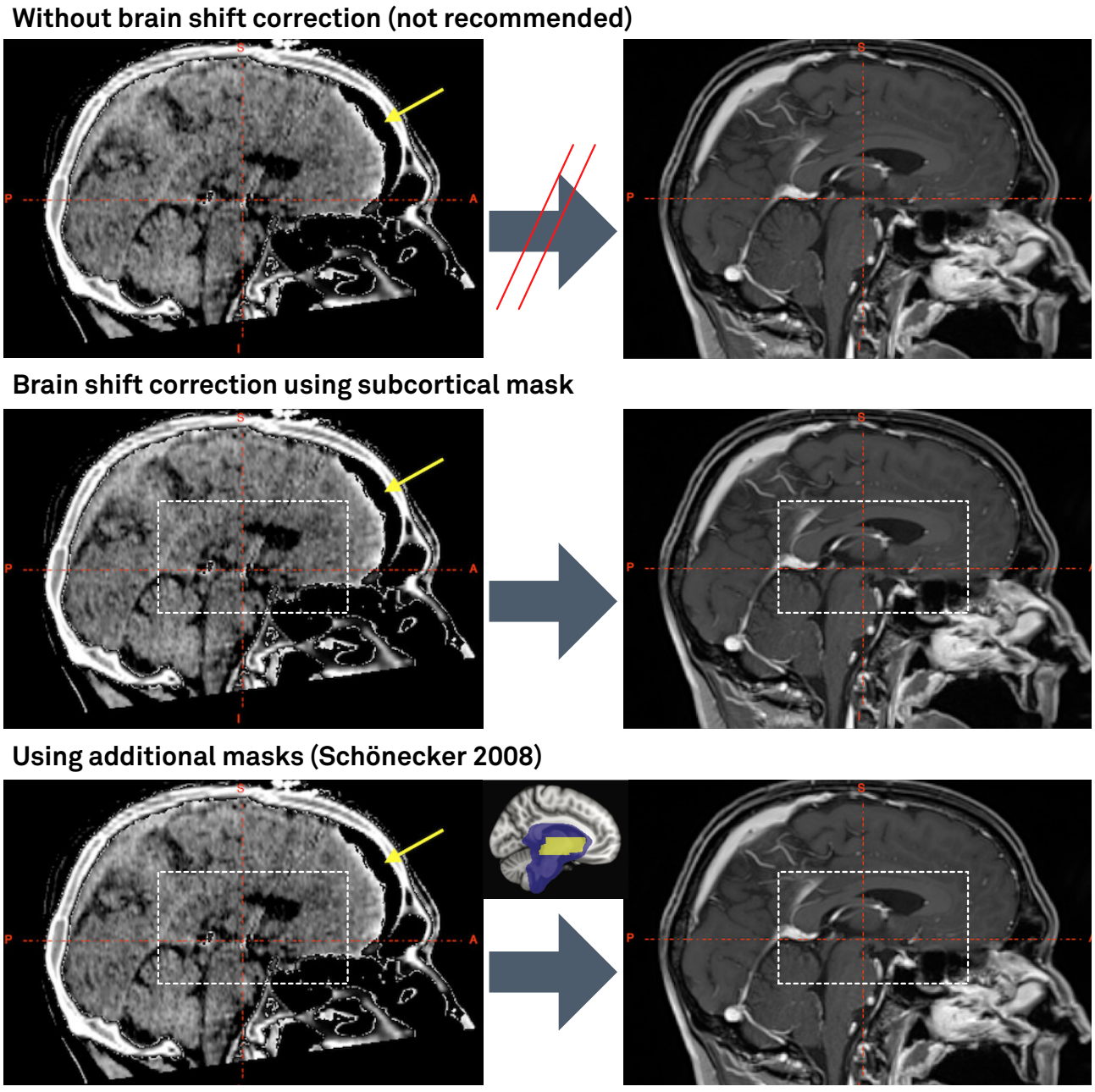

Figure S1: Brain shift correction approach. The top panel shows a whole-brain affine registration aligning a postoperative CT with frontal pneumocephalus (left) to a preoperative T1-weighted MRI (post gadolinium). Based on the pneumocephalus (yellow arrow), a nonlinear error results that is largest in frontal regions (at the site of the pneumocephalus) that may still be substantial in the regions of interest of DBS (figure 4). In the mid row, an additional refinement transform between the subcortical area delineated by the white dashed box is computed. Finally, in the third row, one or two additional refinement transforms between subcortical areas of interest are computed based on masks defined in (Schönecker et al., 2009). This approach gradually shifts the registration area away from the area nonlinearly distorted by pneumocephalus toward the subcortical regions of interest.

References

Accolla, E.A., Herrojo Ruiz, M., Horn, A., Schneider, G.-H., Schmitz-Hubsch, T., Draganski, B., Kühn, A.A., 2016. Brain networks modulated by subthalamic nucleus deep brain stimulation. Brain 139, 2503–2515. doi:10.1093/brain/aww182

Accolla, E.A., Horn, A., Herrojo Ruiz, M., Neumann, W.-J., Kühn, A.A., 2017. Reply: Oscillatory coupling of the subthalamic nucleus in obsessive compulsive disorder. Brain 140, e57–e57. doi:10.1093/brain/awx165

Ahsan, R.L., Allom, R., Gousias, I.S., Habib, H., Turkheimer, F.E., Free, S., Lemieux, L., Myers, R., Duncan, J.S., Brooks, D.J., 2007. Volumes, spatial extents and a probabilistic atlas of the human basal ganglia and thalamus 38, 261–270. doi: 10.1016/j.neuroimage.2007.06.004

Akram, H., Dayal, V., Mahlknecht, P., Georgiev, D., Hyam, J., Foltynie, T., Limousin, P., De Vita, E., Jahanshahi, M., Ashburner, J., Behrens, T., Hariz, M., Zrinzo, L., 2018. Connectivity derived thalamic segmentation in deep brain stimulation for tremor. Neuroimage Clin 18, 130–142. doi:10.1016/j.nicl.2018.01.008

Akram, H., Sotiropoulos, S.N., Jbabdi, S., Georgiev, D., Mahlknecht, P., Hyam, J., Foltynie, T., Limousin, P., De Vita, E., Jahanshahi, M., Hariz, M., Ashburner, J., Behrens, T., Zrinzo, L., 2017. Subthalamic deep brain stimulation sweet spots and hyperdirect cortical connectivity in Parkinson's disease. NeuroImage 158, 332–345. doi: 10.1016/j.neuroimage.2017.07.012

Alho, A.T.D.L., Hamani, C., Alho, E.J.L., da Silva, R.E., Santos, G.A.B., Neves, R.C., Carreira, L.L., Araújo, C.M.M., Magalhães, G., Coelho, D.B., Alegro, M.C., Martin, M.G.M., Grinberg, L.T., Pasqualucci, C.A., Heinsen, H., Fonoff, E.T., Amaro, E., 2017. Magnetic resonance diffusion tensor imaging for the pedunculopontine nucleus: proof of concept and histological correlation. Brain Structure and Function 12, 26–12. doi:10.1007/s00429-016-1356-0

Alho, E.J.L., Di Lorenzo Alho, A.T., Grinberg, L., Amaro, E., Santos, G.A.B., Silva, R.E., Neves, R.C., Alegro, M., Coelho, D.B., Teixeira, M.J., Fonoff, E.T., Heinsen, H., 2017. High thickness histological sections as alternative to study the three-dimensional microscopic human sub-cortical neuroanatomy Eduardo Joaquim Lopes Alho, Ana Tereza Di Lorenzo Alho, Lea Grinberg, Edson Amaro, Gláucia Aparecida Bento dos Santos, et al. Brain Structure and Function 1–14. doi:10.1007/s00429-017-1548-2

Amunts, K., Lepage, C., Borgeat, L., Mohlberg, H., Dickscheid, T., Rousseau, M.-É., Bludau, S., Bazin, P.-L., Lewis, L.B., Oros-Peusquens, A.-M., Shah, N.J., Lippert, T., Zilles, K., Evans, A.C., 2013. BigBrain: an ultrahigh-resolution 3D human brain model. Science 340, 1472–1475. doi:10.1126/science.1235381

Amunts, K., Schleicher, A., Zilles, K., 2007. Cytoarchitecture of the cerebral cortex--more than localization. NeuroImage 37, 1061–5– discussion 1066–8. doi:10.1016/j.neuroimage.2007.02.037

Andersson, J.L.R., Smith, S., 2010. Non-linear registration, aka spatial normalisation. FMRIB technical report 1–22.

Archer, D.B., Vaillancourt, D.E., Coombes, S.A., 2017. A Template and Probabilistic Atlas of the Human Sensorimotor Tracts using Diffusion MRI. Cerebral Cortex 1–15. doi: 10.1093/cercor/bhx066

Ashburner, J., 2007. A fast diffeomorphic image registration algorithm. 38, 95–113. doi: 10.1016/j.neuroimage.2007.07.007

Ashburner, J., Friston, K.J., 2011. Diffeomorphic registration using geodesic shooting and Gauss–Newton optimisation. NeuroImage 55, 954–967. doi:10.1016/j.neuroimage.2010.12.049

Ashburner, J., Friston, K.J., 2005. Unified segmentation. 26, 839–851. doi:10.1016/j.neuroimage.2005.02.018

Auzias, G., Coulon, O., Brovelli, A., 2016. MarsAtlas: A cortical parcellation atlas for functional mapping. Hum Brain Mapp. doi:10.1002/hbm.23121

Auzias, G., Lefèvre, J., Le Troter, A., Fischer, C., Perrot, M., Régis, J., Coulon, O., 2013. Model-Driven Harmonic Parameterization of the Cortical Surface: HIP-HOP. IEEE Trans Med Imaging 32, 873–887.

Avants, B.B., Epstein, C.L., Grossman, M., Gee, J.C., 2008. Symmetric diffeomorphic image registration with cross-correlation: evaluating automated labeling of elderly and neurodegenerative brain. Med Image Anal 12, 26–41. doi:10.1016/j.media.2007.06.004

Axer, M., Amunts, K., Grässel, D., Palm, C., Dammers, J., Axer, H., Pietrzyk, U., Zilles, K., 2011. A novel approach to the human connectome: ultra-high resolution mapping of fiber tracts in the brain. 54, 1091–1101. doi:10.1016/j.neuroimage.2010.08.075

Åström, M., Diczfalusy, E., Martens, H., Wårdell, K., 2014. Relationship between Neural Activation and Electric Field Distribution during Deep Brain Stimulation. IEEE Trans. Biomed. Eng. 1–1. doi:10.1109/TBME.2014.2363494

Åström, M., Zrinzo, L.U., Tisch, S., Tripoliti, E., Hariz, M.I., Wårdell, K., 2009. Method for patient-specific finite element modeling and simulation of deep brain stimulation. Med Biol Eng Comput 47, 21–28. doi:10.1007/s11517-008-0411-2

Baldermann, J.C., Kohl, S., Visser-Vandewalle, V., Klehr, M., Huys, D., Kuhn, J., 2016. Deep Brain Stimulation of the Ventral Capsule/Ventral Striatum Reproducibly Improves Symptoms of Body Dysmorphic Disorder. Brain Stimul. doi:10.1016/j.brs.2016.09.003

Barow, E., Neumann, W.-J., Brücke, C., Huebl, J., Horn, A., Brown, P., Krauss, J.K., Schneider, G.-H., Kühn, A.A., 2014. Deep brain stimulation suppresses pallidal low frequency activity in patients with phasic dystonic movements. Brain 137, 3012–3024. doi:10.1093/brain/awu258

Behrens, T.E.J., Johansen-Berg, H., Woolrich, M.W., Smith, S.M., Wheeler-Kingshott, C.A.M., Boulby, P.A., Barker, G.J., Sillery, E.L., Sheehan, K., Ciccarelli, O., Thompson, A.J., Brady, J.M., Matthews, P.M., 2003. Non-invasive mapping of connections between human thalamus and cortex using diffusion imaging. 6, 750–757. doi:10.1038/nn1075

Boes, A.D., Prasad, S., Liu, H., Liu, Q., Pascual-Leone, A., Caviness, V.S., Jr, Fox, M.D., 2015. Network localization of neurological symptoms from focal brain lesions. Brain 138, 3061–3075. doi:10.1093/brain/awv228

Bonmassar, G., Angelone, L.M., Makris, N., 2014. A Virtual Patient Simulator Based on Human Connectome and 7 T MRI for Deep Brain Stimulation. International journal on advances in life sciences 6, 364–372.

Brücke, C., Horn, A., Huppke, P., Kupsch, A., Schneider, G.-H., Kühn, A.A., 2014. Failure of Pallidal Deep Brain Stimulation in a Case of Rapid-Onset Dystonia Parkinsonism (DYT12). Movement Disorders Clinical Practice n/a–n/a. doi:10.1002/mdc3.12124

Buckner, R.L., Krienen, F.M., Castellanos, A., Diaz, J.C., Yeo, B.T.T., 2011. The organization of the human cerebellum estimated by intrinsic functional connectivity. J Neurophysiol 106, 2322–2345. doi:10.1152/jn.00339.2011

Butson, C.R., Cooper, S.E., Henderson, J.M., McIntyre, C.C., 2006. Predicting the effects of deep brain stimulation with diffusion tensor based electric field models. Med Image Comput Comput Assist Interv 9, 429–437.

Butson, C.R., Cooper, S.E., Henderson, J.M., Wolgamuth, B., McIntyre, C.C., 2011. Probabilistic analysis of activation volumes generated during deep brain stimulation. 54, 2096–2104. doi:10.1016/j.neuroimage.2010.10.059

Butson, C.R., McIntyre, C.C., 2008. Current steering to control the volume of tissue activated during deep brain stimulation. Brain Stimul 1, 7–15. doi:10.1016/j.brs.2007.08.004

Buzsáki, G., 2006. Rhythms of the Brain. Oxford University Press.

Caire, F., Ranoux, D., Guehl, D., Burbaud, P., Cuny, E., 2013. A systematic review of studies on anatomical position of electrode contacts used for chronic subthalamic stimulation in Parkinson's disease. Acta Neurochir (Wien) 155, 1647–54–discussion 1654. doi:10.1007/s00701-013-1782-1

Cameron Craddock, R., S Margulies, D., Bellec, P., Nolan Nichols, B., Alcauter, S., A Barrios, F., Burnod, Y., J Cannistraci, C., Cohen-Adad, J., De Leener, B., Dery, S., Downar, J., Dunlop, K., R Franco, A., Seligman Froehlich, C., J Gerber, A., S Ghosh, S., J Grabowski, T., Hill, S., Sólon Heinsfeld, A., Matthew Hutchison, R., Kundu, P., R Laird, A., Liew, S.-L., J Lurie, D., G McLaren, D., Meneguzzi, F., Mennes, M., Mesmoudi, S., O'Connor, D., H Pasaye, E., Peltier, S., Poline, J.-B., Prasad, G., Fraga Pereira, R., Quirion, P.-O., Rokem, A., S Saad, Z., Shi, Y., C Strother, S., Toro, R., Q Uddin, L., D Van Horn, J., W Van Meter, J., C Welsh, R., Xu, T., 2016. Brainhack: a collaborative workshop for the open neuroscience community. Gigascience 5, 16. doi:10.1186/s13742-016-0121-x

Chakravarty, M.M., Bertrand, G., Hodge, C.P., Sadikot, A.F., Collins, D.L., 2006. The creation of a brain atlas for image guided neurosurgery using serial histological data. NeuroImage 30, 359–376. doi:10.1016/j.neuroimage.2005.09.041

Chakravarty, M.M., Sadikot, A.F., Germann, J., Bertrand, G., Collins, D.L., 2008. Towards a validation of atlas warping techniques. Med Image Anal 12, 713–726. doi:10.1016/j.media.2008.04.003

Chakravarty, M.M., Steadman, P., van Eede, M.C., Calcott, R.D., Gu, V., Shaw, P., Raznahan, A., Collins, D.L., Lerch, J.P., 2012. Performing label-fusion-based segmentation using multiple automatically generated templates. Hum Brain Mapp 34, 2635–2654. doi:10.1002/hbm.22092

Chaturvedi, A., Luján, J.L., McIntyre, C.C., 2013. Artificial neural network based characterization of the volume of tissue activated during deep brain stimulation. J Neural Eng 10, 056023. doi:10.1088/1741-2560/10/5/056023

Choi, E.Y., Yeo, B.T.T., Buckner, R.L., 2012. The organization of the human striatum estimated by intrinsic functional connectivity. J Neurophysiol 108, 2242–2263. doi:10.1152/jn.00270.2012

Craddock, R.C., James, G.A., Holtzheimer, P.E., Hu, X.P., Mayberg, H.S., 2012. A whole brain fMRI atlas generated via spatially constrained spectral clustering. Hum Brain Mapp 33, 1914–1928. doi:10.1002/hbm.21333

da Silva, N.M., Ahmadi, S.-A., Tafula, S.N., Cunha, J.P.S., Bötzel, K., Vollmar, C., Rozanski, V.E., 2016. A diffusion-based connectivity map of the GPi for optimised stereotactic targeting in DBS. NeuroImage 1–9. doi:10.1016/j.neuroimage.2016.06.018

da Silva, N.M., Rozanski, V.E., Cunha, J.P.S., 2015. A 3D multimodal approach to precisely locate DBS electrodes in the basal ganglia brain region, in:. Presented at the 2015 7th International IEEE/EMBS Conference on Neural Engineering (NER), pp. 292–295. doi:10.1109/NER.2015.7146617

Dale, A.M., Fischl, B., Sereno, M.I., 1999. Cortical surface-based analysis. I. Segmentation and surface reconstruction. NeuroImage 9, 179–194. doi:10.1006/nimg.1998.0395

Darby, R., Laganiere, S., Pascual-Leone, A., Prasad, S., Fox, M.D., 2016. Finding the imposter: brain connectivity of lesions causing delusional misidentifications. Brain 1–11. doi:10.1093/brain/aww288

Darby, R.R., Horn, A., Cushman, F., Fox, M.D., 2017. Lesion network localization of criminal behavior. Proc Natl Acad Sci USA 56, 201706587–6. doi:10.1073/pnas.1706587115

Dembek, T.A., Barbe, M.T., Åström, M., Hoevels, M., Visser-Vandewalle, V., Fink, G.R., Timmermann, L., 2017. Probabilistic mapping of deep brain stimulation effects in essential tremor. Neuroimage Clin 13, 164–173. doi:10.1016/j.nicl.2016.11.019

Desikan, R.S., Ségonne, F., Fischl, B., Quinn, B.T., Dickerson, B.C., Blacker, D., Buckner, R.L., Dale, A.M., Maguire, R.P., Hyman, B.T., Albert, M.S., Killiany, R.J., 2006. An automated labeling system for subdividing the human cerebral cortex on MRI scans into gyral based regions of interest. NeuroImage 31, 968–980. doi:10.1016/j.neuroimage.2006.01.021

Destrieux, C., Fischl, B., Dale, A., Halgren, E., 2010. Automatic parcellation of human cortical gyri and sulci using standard anatomical nomenclature. NeuroImage 53, 1–15. doi:10.1016/j.neuroimage.2010.06.010

Diedrichsen, J., 2006. A spatially unbiased atlas template of the human cerebellum. NeuroImage 33, 127–138. doi:10.1016/j.neuroimage.2006.05.056

Diedrichsen, J., Maderwald, S., Küper, M., Thürling, M., Rabe, K., Gizewski, E.R., Ladd, M.E., Timmann, D., 2011. Imaging the deep cerebellar nuclei: a probabilistic atlas and normalization procedure. NeuroImage 54, 1786–1794. doi:10.1016/j.neuroimage.2010.10.035

Dormont, D., Seidenwurm, D., Galanaud, D., Cornu, P., Yelnik, J., & Bardinet, E., 2010. Neuroimaging and Deep Brain Stimulation. AJNR American Journal of Neuroradiology, 31(1), 15–23. http://doi.org/10.3174/ajnr.A1644

D'Albis, T., Haegelen, C., Essert, C., Fernandez-Vidal, S., Lalys, F., Jannin, P., 2014. PyDBS: an automated image processing workflow for deep brain stimulation surgery. - PubMed - NCBI. Int J CARS 10, 117–128.

Ehlen, F., Vonberg, I., Tiedt, H.O., Horn, A., Fromm, O., Kühn, A.A., Klostermann, F., 2017. Thalamic deep brain stimulation decelerates automatic lexical activation. Brain Cogn 111, 34–43. doi:10.1016/j.bandc.2016.10.001

Edlow, B.L., Takahashi, E., Wu, O., Benner, T., Dai, G., Bu, L., Grant, P.E., Greer, D.M., Greenberg, S.M., Kinney, H.C., Folkerth, R.D., 2012. Neuroanatomic connectivity of the human ascending arousal system critical to consciousness and its disorders. J. Neuropathol. Exp. Neurol. 71, 531–546. doi:10.1097/NEN.0b013e3182588293

Eickhoff, S.B., Heim, S., Zilles, K., Amunts, K., 2006. Testing anatomically specified hypotheses in functional imaging using cytoarchitectonic maps. NeuroImage 32, 570–582. doi:10.1016/j.neuroimage.2006.04.204

Eickhoff, S.B., Jbabdi, S., Caspers, S., Laird, A.R., Fox, P.T., Zilles, K., Behrens, T.E.J., 2010. Anatomical and functional connectivity of cytoarchitectonic areas within the human parietal operculum. 30, 6409–6421. doi:10.1523/JNEUROSCI.5664-09.2010

Eickhoff, S.B., Stephan, K.E., Mohlberg, H., Grefkes, C., Fink, G.R., Amunts, K., Zilles, K., 2005. A new SPM toolbox for combining probabilistic cytoarchitectonic maps and functional imaging data. 25, 1325–1335. doi:10.1016/j.neuroimage.2004.12.034

Eisenstein, S.A., Koller, J.M., Black, K.D., Campbell, M.C., Lugar, H.M., Ushe, M., Tabbal, S.D., Karimi, M., Hershey, T., Perlmutter, J.S., Black, K.J., 2014. Functional anatomy of subthalamic nucleus stimulation in Parkinson disease. Ann Neurol 76, 279–295. doi:10.1002/ana.24204

Ewert, S., Horn, A., Finkel, F., Li, N., Kühn, A.A., Herrington, T.M., 2018a. Toward optimized nonlinear deformation algorithms for subcortical DBS target regions in

MRI, in:. Presented at the Deutsche Gesellschaft für Klinische Neurophysiologie und Funktionelle Bildgebung.

Ewert, S., Plettig, P., Li, N., Chakravarty, M.M., Collins, D.L., Herrington, T.M., Kühn, A.A., Horn, A., 2018b. Toward defining deep brain stimulation targets in MNI space: A subcortical atlas based on multimodal MRI, histology and structural connectivity. NeuroImage 170, 271–282. doi:10.1016/j.neuroimage.2017.05.015

Fan, L., Li, H., Zhuo, J., Zhang, Y., Wang, J., Chen, L., Yang, Z., Chu, C., Xie, S., Laird, A.R., Fox, P.T., Eickhoff, S.B., Yu, C., Jiang, T., 2016. The Human Brainnetome Atlas: A New Brain Atlas Based on Connectional Architecture. Cereb. Cortex 26, 3508–3526. doi:10.1093/cercor/bhw157

Fasano, A., Laganiere, S.E., Lam, S., Fox, M.D., 2017. Lesions causing freezing of gait localize to a cerebellar functional network. Ann Neurol 81, 129–141. doi:10.1002/ana.24845

Fedorov, A., Beichel, R., Kalpathy-Cramer, J., Finet, J., Fillion-Robin, J.-C., Pujol, S., Bauer, C., Jennings, D., Fennessy, F., Sonka, M., Buatti, J., Aylward, S., Miller, J.V., Pieper, S., Kikinis, R., 2012. 3D Slicer as an image computing platform for the Quantitative Imaging Network. Magn Reson Imaging 30, 1323–1341. doi:10.1016/j.mri.2012.05.001

Fillard, P., Descoteaux, M., Goh, A., Gouttard, S., Jeurissen, B., Malcolm, J., Ramirez-Manzanares, A., Reisert, M., Sakaie, K., Tensaouti, F., Yo, T., Mangin, J.-F., Poupon, C., 2011. Quantitative evaluation of 10 tractography algorithms on a realistic diffusion MR phantom 56, 220–234. doi:10.1016/j.neuroimage.2011.01.032

Fischer, D.B., Boes, A.D., Demertzi, A., Evrard, H.C., Laureys, S., Edlow, B.L., Liu, H., Saper, C.B., Pascual-Leone, A., Fox, M.D., Geerling, J.C., 2016. A human brain network derived from coma-causing brainstem lesions. 10.1212/WNL.0000000000003404–9. doi:10.1212/WNL.0000000000003404

Fischl, B., van der Kouwe, A., Destrieux, C., Halgren, E., Ségonne, F., Salat, D.H., Busa, E., Seidman, L.J., Goldstein, J., Kennedy, D., Caviness, V., Makris, N., Rosen, B., Dale, A.M., 2004. Automatically parcellating the human cerebral cortex. Cerebral Cortex 14, 11–22. doi:10.1093/cercor/bhg087

Frazier, J.A., Chiu, S., Breeze, J.L., Makris, N., Lange, N., Kennedy, D.N., Herbert, M.R., Bent, E.K., Koneru, V.K., Dieterich, M.E., Hodge, S.M., Rauch, S.L., Grant, P.E., Cohen, B.M., Seidman, L.J., Caviness, V.S., Biederman, J., 2005. Structural Brain Magnetic Resonance Imaging of Limbic and Thalamic Volumes in Pediatric Bipolar Disorder. Am J Psychiatry 1–10. doi:10.1176/appi.ajp.162.7.1256

Friston, K.J., Holmes, A.P., Worsley, K.J., Poline, J.P., Frith, C.D., Frackowiak, R.S.J., 2004. Statistical parametric maps in functional imaging: A general linear approach. Hum Brain Mapp 2, 189–210. doi:10.1002/hbm.460020402

Fonov, V.S., Evans, A.C., McKinstry, R.C., Almli, C.R., Collins, D.L., 2009. Unbiased nonlinear average age-appropriate brain templates from birth to adulthood. NeuroImage 47, S102.

Forel, A., 1877. Untersuchungen über die Haubenregion und ihre oberen verknüpfungen im Gehirne des Menschen und einiger Säugethiere.

Forstmann, B.U., Isaacs, B.R., Temel, Y., 2017. Ultra High Field MRI-Guided Deep Brain Stimulation. Trends in Biotechnology 35, 904–907. doi:10.1016/j.tibtech.2017.06.010

Forstmann, B.U., Keuken, M.C., Alkemade, A., 2016. The next step for imaging the subthalamic nucleus. Brain aww245–2. doi:10.1093/brain/aww245

Forstmann, B.U., Keuken, M.C., Schäfer, A., Bazin, P.-L., Alkemade, A., Turner, R., 2014. Multi-modal ultra-high resolution structural 7-Tesla MRI data repository. Sci. Data 1, 140050–8. doi:10.1038/sdata.2014.50

Garcia-Garcia, D., Guridi, J., Toledo, J.B., Alegre, M., Obeso, J.A., Rodríguez-Oroz, M.C., 2016. Stimulation sites in the subthalamic nucleus and clinical improvement in Parkinson's disease: a new approach for active contact localization. http://dx.doi.org/10.3171/2015.9.JNS15868 1–12. doi:10.3171/2015.9.JNS15868

Gaser, C., 2016. CAT-a computational anatomy toolbox for the analysis of structural MRI data. Organization for Human Brain Mapping.

Geng, X., Xu, X., Horn, A., Li, N., Ling, Z., Brown, P., Wang, S., 2018. Intra-operative characterisation of subthalamic oscillations in Parkinson's disease. Clinical Neurophysiology 0. doi:10.1016/j.clinph.2018.01.075

Glasser, M.F., Coalson, T.S., Robinson, E.C., Hacker, C.D., Harwell, J., Yacoub, E., Uğurbil, K., Andersson, J., Beckmann, C.F., Jenkinson, M., Smith, S.M., Van Essen, D.C., 2016. A multi-modal parcellation of human cerebral cortex. Nature. doi:10.1038/nature18933

Goldstein, J.M., Seidman, L.J., Makris, N., Ahern, T., O'Brien, L.M., Caviness, V.S., Kennedy, D.N., Faraone, S.V., Tsuang, M.T., 2007. Hypothalamic abnormalities in schizophrenia: sex effects and genetic vulnerability. BPS 61, 935–945. doi:10.1016/j.biopsych.2006.06.027

Gordon, E.M., Laumann, T.O., Adeyemo, B., Huckins, J.F., Kelley, W.M., Petersen, S.E., 2016. Generation and Evaluation of a Cortical Area Parcellation from Resting-State Correlations. Cereb. Cortex 26, 288–303. doi:10.1093/cercor/bhu239

Gousias, I.S., Rueckert, D., Heckemann, R.A., Dyet, L.E., Boardman, J.P., Edwards, A.D., Hammers, A., 2008. Automatic segmentation of brain MRIs of 2-year-olds into 83 regions of interest. NeuroImage 40, 672–684. doi:10.1016/j.neuroimage.2007.11.034

Gunalan, K., Chaturvedi, A., Howell, B., Duchin, Y., Lempka, S.F., Patriat, R., Sapiro, G., Harel, N., McIntyre, C.C., 2017. Creating and parameterizing patient-specific deep brain stimulation pathway-activation models using the hyperdirect pathway as an example. PLoS ONE 12, e0176132. doi:10.1371/journal.pone.0176132

Hammers, A., Allom, R., Koepp, M.J., Free, S.L., Myers, R., Lemieux, L., Mitchell, T.N., Brooks, D.J., Duncan, J.S., 2003. Three-dimensional maximum probability atlas of the human brain, with particular reference to the temporal lobe. Hum Brain Mapp 19, 224–247. doi:10.1002/hbm.10123

Hasgall, P.A., Di Gennaro F, Baumgartner, C., Neufeld, E., Gosselin, M.C., Payne, D., Klingenböck, A., Kuster, N., 2015. IT'IS Database for thermal and electromagnetic parameters of biological tissues. doi:DOI: 10.13099/VIP21000-03-0

Hell, F., Taylor, P.C.J., Mehrkens, J.H., Bötzel, K., 2018a. Subthalamic stimulation, oscillatory activity and connectivity reveal functional role of STN and network mechanisms during decision making under conflict. NeuroImage. doi:10.1016/j.neuroimage.2018.01.001

Hell, F., Plate, A., Mehrkens, J. H., & Bötzel, K., 2018b. Subthalamic oscillatory activity and connectivity during gait in Parkinson's disease. NeuroImage. Clinical, 19, 396–405. http://doi.org/10.1016/j.nicl.2018.05.001

Hemm, S., Coste, J., Gabrillargues, J., Ouchchane, L., Sarry, L., Caire, F., Vassal, F., Nuti, C., Derost, P., Durif, F., Lemaire, J.-J., 2009. Contact position analysis of deep brain stimulation electrodes on post-operative CT images. Acta Neurochir (Wien) 151, 823–829. doi:10.1007/s00701-009-0393-3

Hemm, S., Mennessier, G., Vayssiere, N., Cif, L., Coubes, P., 2005. Co-registration of stereotactic MRI and isofieldlines during deep brain stimulation. Brain Res Bull 68, 59–61. doi:10.1016/j.brainresbull.2005.08.024

Hohlefeld, F.U., Ehlen, F., Tiedt, H.O., Krugel, L.K., Horn, A., Kühn, A.A., Curio, G., Klostermann, F., Nikulin, V.V., 2015. Correlation between cortical and subcortical

neural dynamics on multiple time scales in Parkinson's disease. Neuroscience 298, 145–160. doi:10.1016/j.neuroscience.2015.04.013

Hohlefeld, F.U., Ewald, A., Ehlen, F., Tiedt, H.O., Horn, A., Kühn, A.A., Curio, G., Klostermann, F., Nikulin, V.V., 2017. Neural correlates of lexical decisions in Parkinson's disease revealed with multivariate extraction of cortico-subthalamic interactions. Clin Neurophysiol 128, 538–548. doi:10.1016/j.clinph.2016.12.026

Hohlefeld, F.U., Huchzermeyer, C., Huebl, J., Schneider, G.H., Nolte, G., Brücke, C., Schönecker, T., Kühn, A.A., Curio, G., Nikulin, V.V., 2013. Functional and effective connectivity in subthalamic local field potential recordings of patients with Parkinson's disease. Neuroscience 250, 320–332. doi:10.1016/j.neuroscience.2013.07.028

de Hollander, G., Keuken, M. C., Bazin, P.-L., Weiss, M., Neumann, J., Reimann, K., et al., 2014. A gradual increase of iron toward the medial-inferior tip of the subthalamic nucleus. Human Brain Mapping, 35(9), 4440–4449. http://doi.org/10.1002/hbm.22485

Horn, A., 2017. PCA MNI 2009b NLIN template. doi:10.6084/m9.figshare.4644472.v2

Horn, A., 2016. MNI T1 6thGen NLIN to MNI 2009b NLIN ANTs transform. doi:10.6084/m9.figshare.3502238.v2

Horn, A., 2015. A structural group-connectome in standard stereotactic (MNI) space. DiB 5, 292–296. doi:10.1016/j.dib.2015.08.035

Horn, A., Blankenburg, F., 2016. Toward a standardized structural-functional group connectome in MNI space. NeuroImage 124, 310–322. doi:10.1016/j.neuroimage.2015.08.048

Horn, A., Kühn, A.A., 2015. Lead-DBS: a toolbox for deep brain stimulation electrode localizations and visualizations. NeuroImage 107, 127–135. doi:10.1016/j.neuroimage.2014.12.002

Horn, A., Kühn, A.A., Merkl, A., Shih, L., Alterman, R., Fox, M., 2017a. Probabilistic conversion of neurosurgical DBS electrode coordinates into MNI space. NeuroImage 150, 395–404. doi:10.1016/j.neuroimage.2017.02.004

Horn, A., Neumann, W.-J., Degen, K., Schneider, G.-H., Kühn, A.A., 2017b. Toward an electrophysiological “sweet spot” for deep brain stimulation in the subthalamic nucleus. Hum Brain Mapp. doi:10.1002/hbm.23594

Horn, A., Ostwald, D., Reisert, M., Blankenburg, F., 2014. The structural-functional connectome and the default mode network of the human brain. NeuroImage 102 Pt 1, 142–151. doi:10.1016/j.neuroimage.2013.09.069

Horn, A., Reich, M., Vorwerk, J., Li, N., Wenzel, G., Fang, Q., Schmitz-Hubsch, T., Nickl, R., Kupsch, A., Volkmann, J., Kühn, A.A., Fox, M.D., 2017c. Connectivity Predicts deep brain stimulation outcome in Parkinson disease. Ann Neurol 82, 67–78. doi:10.1002/ana.24974

Husch, A., Petersen, M.V., Gemmar, P., Goncalves, J., Hertel, F., 2017. PaCER - A fully automated method for electrode trajectory and contact reconstruction in deep brain stimulation. Neuroimage Clin 17, 80–89. doi:10.1016/j.nicl.2017.10.004

Husch, A., Petersen, M.V., Gemmar, P., Goncalves, J., Sunde, N., Hertel, F., 2018. Post-operative deep brain stimulation assessment: Automatic data integration and report generation. Brain Stimul 1–14. doi:10.1016/j.brs.2018.01.031

Huth, A.G., de Heer, W.A., Griffiths, T.L., Theunissen, F.E., Gallant, J.L., 2016. Natural speech reveals the semantic maps that tile human cerebral cortex. Nature 532, 453–458. doi:10.1038/nature17637

Huth, A.G., Griffiths, T.L., Theunissen, F.E., Gallant, J.L., 2015. PrAGMATiC: a Probabilistic and Generative Model of Areas Tiling the Cortex.

Ilinski, I., Horn, A., Paul-Gilloteaux, P., Gressens, P., Verney, C., Kultas-Ilinsky, K., 2018. Human Motor Thalamus Reconstructed in 3D from Continuous Sagittal Sections with Identified Subcortical Afferent Territories. *epub ahead of print.*

Iwahori, N., 1978. A Golgi study on the subthalamic nucleus of the cat. The Journal of comparative neurology 182, 383–397. doi:10.1002/cne.901820303

Jakab, A., Blanc, R., Berenyi, E.L., Szekely, G., 2012. Generation of Individualized Thalamus Target Maps by Using Statistical Shape Models and Thalamocortical Tractography. AJNR Am J Neuroradiol 33, 2110–2116. doi:10.3174/ajnr.A3140

Jenkinson, M., Bannister, P., Brady, M., Smith, S., 2002. Improved optimization for the robust and accurate linear registration and motion correction of brain images. 17, 825–841. doi:10.1006/nimg.2002.1132

Johnson, H., Harris, G., Williams, K., 2007. BRAINSFit: mutual information rigid registrations of whole-brain 3D images, using the insight toolkit. Insight J.

Joliot, M., Jobard, G., Naveau, M., Delcroix, N., Petit, L., Zago, L., Crivello, F., Mellet, E., Mazoyer, B., Tzourio-Mazoyer, N., 2015. AICHA: An atlas of intrinsic connectivity of homotopic areas. J. Neurosci. Methods 254, 46–59. doi:10.1016/j.jneumeth.2015.07.013

Kellner, E., Dhital, B., Kiselev, V.G., Reisert, M., 2015. Gibbs-ringing artifact removal based on local subvoxel-shifts. Magnetic Resonance in Medicine n/a–n/a. doi:10.1002/mrm.26054

Keuken, M.C., Bazin, P.-L., Schäfer, A., Neumann, J., Turner, R., Forstmann, B.U., 2013. Ultra-high 7T MRI of structural age-related changes of the subthalamic nucleus. J Neurosci 33, 4896–4900. doi:10.1523/JNEUROSCI.3241-12.2013

Keuken, M.C., Bazin, P.L., Crown, L., Hootsmans, J., Laufer, A., Müller-Axt, C., Sier, R., van der Putten, E.J., Schäfer, A., Turner, R., Forstmann, B.U., 2014. Quantifying inter-individual anatomical variability in the subcortex using 7 T structural MRI. NeuroImage 94, 40–46. doi:10.1016/j.neuroimage.2014.03.032

Kita, T., Kita, H., 2012. The subthalamic nucleus is one of multiple innervation sites for long-range corticofugal axons: a single-axon tracing study in the rat. J Neurosci 32, 5990–5999. doi:10.1523/JNEUROSCI.5717-11.2012

Klein, A., Andersson, J., Ardekani, B.A., Ashburner, J., Avants, B., Chiang, M.-C., Christensen, G.E., Collins, D.L., Gee, J., Hellier, P., Song, J.H., Jenkinson, M., Lepage, C., Rueckert, D., Thompson, P., Vercauteren, T., Woods, R.P., Mann, J.J., Parsey, R.V., 2009. Evaluation of 14 nonlinear deformation algorithms applied to human brain MRI registration. NeuroImage 46, 786–802. doi:10.1016/j.neuroimage.2008.12.037

Konopleva, L., Il'yasov, K.A., Skibbe, H., Kiselev, V.G., Kellner, E., Dhital, B., Reisert, M., 2018. Modelfree global tractography. NeuroImage. doi:10.1016/j.neuroimage.2018.03.058

Krause, P., Brüggemann, N., Völzmann, S., Horn, A., Kupsch, A., Schneider, G.H., Lohmann, K., Kühn, A., 2015. Long-term effect on dystonia after pallidal deep brain stimulation (DBS) in three members of a family with a THAP1 mutation. J Neurol 262, 2739–2744. doi:10.1007/s00415-015-7908-z

Krause, P., Lauritsch, K., Lipp, A., Horn, A., Weschke, B., Kupsch, A., Kiening, K.L., Schneider, G.H., Kühn, A.A., 2016. Long-term results of deep brain stimulation in a cohort of eight children with isolated dystonia. J Neurol 263, 2319–2326. doi:10.1007/s00415-016-8253-6

Kroneberg, D., Plettig, P., Schneider, G.-H., Kühn, A.A., 2017. Motor Cortical Plasticity Relates to Symptom Severity and Clinical Benefit From Deep Brain Stimulation in Cervical Dystonia. Neuromodulation: Technology at the Neural Interface 27, 1789. doi:10.1111/ner.12690

Krauth, A., Blanc, R., Poveda, A., Jeanmonod, D., Morel, A., Székely, G., 2010. A mean three-dimensional atlas of the human thalamus: generation from multiple histological data. NeuroImage 49, 2053–2062. doi:10.1016/j.neuroimage.2009.10.042

Kreher, B.W., Mader, I., Kiselev, V.G., 2008. Gibbs tracking: a novel approach for the reconstruction of neuronal pathways. Magn Reson Med 60, 953–963. doi:10.1002/mrm.21749

Kuncel, A.M., Cooper, S.E., Grill, W.M., 2008. A method to estimate the spatial extent of activation in thalamic deep brain stimulation. Clin Neurophysiol 119, 2148–2158. doi:10.1016/j.clinph.2008.02.025

Laganiere, S., Boes, A.D., Fox, M.D., 2016. Network localization of hemichorea-hemiballismus 86, 2187–2195. doi:10.1212/WNL.0000000000002741

Lauro, P.M., Vanegas Arroyave, N., Huang, L., Taylor, P.A., Zaghloul, K.A., Lungu, C., Saad, Z.S., Horovitz, S.G., 2015. DBSproc: An open source process for DBS electrode localization and tractographic analysis. Hum Brain Mapp n/a–n/a. doi:10.1002/hbm.23039

Li, X., Morgan, P.S., Ashburner, J., Smith, J., Rorden, C., 2016. The first step for neuroimaging data analysis: DICOM to NIfTI conversion. J. Neurosci. Methods 264, 47–56. doi:10.1016/j.jneumeth.2016.03.001

Litvak, V., Jha, A., Eusebio, A., Oostenveld, R., Foltynie, T., Limousin, P., Zrinzo, L., Hariz, M.I., Friston, K., Brown, P., 2011. Resting oscillatory cortico-subthalamic connectivity in patients with Parkinson's disease. Brain 134, 359–374. doi:10.1093/brain/awq332

Lofredi, R., Neumann, W.-J., Bock, A., Horn, A., Huebl, J., Siegert, S., Schneider, G.-H., Krauss, J.K., Kühn, A.A., 2018. Dopamine-dependent scaling of subthalamic gamma bursts with movement velocity in patients with Parkinson's disease. Elife 7, e31895. doi:10.7554/eLife.31895

Lorio, S., Fresard, S., Adaszewski, S., Kherif, F., Chowdhury, R., Frackowiak, R.S., Ashburner, J., Helms, G., Weiskopf, N., Lutti, A., Draganski, B., 2016. New tissue priors for improved automated classification of subcortical brain structures on MRI. NeuroImage 130, 157–166. doi:10.1016/j.neuroimage.2016.01.062

Maier-Hein, K.H., Neher, P.F., Houde, J.-C., Cote, M.-A., Garyfallidis, E., Zhong, J., Chamberland, M., Yeh, F.-C., Lin, Y.C., Ji, Q., Reddick, W.E., Glass, J.O., Chen, D.Q., Feng, Y., Gao, C., Wu, Y., Ma, J., Renjie, H., Li, Q., Westin, C.-F., Deslauriers-Gauthier, S., Gonzalez, J.O.O., Paquette, M., St-Jean, S., Girard, G., Rheault, F., Sidhu, J., Tax, C.M.W., Guo, F., Mesri, H.Y., David, S., Froeling, M., Heemskerk, A.M., Leemans, A., Bore, A., Pinsard, B., Bedetti, C., Desrosiers, M., Brambati, S., Doyon, J., Sarica, A., Vasta, R., Cerasa, A., Quattrone, A., Yeatman, J., Khan, A.R., Hodges, W., Alexander, S., Romascano, D., Barakovic, M., Auria, A., Esteban, O., Lemkaddem, A., Thiran, J.-P., Cetingul, H.E., Odry, B.L., Mailhe, B., Nadar, M.S., Pizzagalli, F., Prasad, G., Villalon-Reina, J.E., Galvis, J., Thompson, P.M., De Santiago Requejo, F., Laguna, P.L., Lacerda, L.M., Barrett, R., Dell'Acqua, F., Catani, M., Petit, L., Caruyer, E., Daducci, A., Dyrby, T.B., Holland-Letz, T., Hilgetag, C.C., Stieltjes, B., Descoteaux, M., 2017. The challenge of mapping the human connectome based on diffusion tractography. Nature Communications 2017 8:1 8, 1349. doi:10.1038/s41467-017-01285-x

Makris, N., Goldstein, J.M., Kennedy, D., Hodge, S.M., Caviness, V.S., Faraone, S.V., Tsuang, M.T., Seidman, L.J., 2006. Decreased volume of left and total anterior insular lobule in schizophrenia. Schizophrenia Research 83, 155–171. doi:10.1016/j.schres.2005.11.020

Marani, E., Heida, T., Lakke, E.A.J.F., Usunoff, K.G., 2008. The Subthalamic Nucleus. Springer Science & Business Media, Berlin, Heidelberg. doi: 10.1007/978-3-540-79462-2

Marek, K., Jennings, D., Lasch, S., Siderowf, A., Tanner, C., Simuni, T., Coffey, C., Kieburtz, K., Flagg, E., Chowdhury, S., Poewe, W., Mollenhauer, B., Klinik, P.-E., Sherer, T., Frasier, M., Meunier, C., Rudolph, A., Casaceli, C., Seibyl, J., Mendick, S., Schuff, N., Zhang, Y., Toga, A., Crawford, K., Ansbach, A., De Blasio, P., Piovella, M., Trojanowski, J., Shaw, L., Singleton, A., Hawkins, K., Eberling, J., Brooks, D., Russell, D., Leary, L., Factor, S., Sommerfeld, B., Hogarth, P., Pighetti, E., Williams, K., Standaert, D., Guthrie, S., Hauser, R., Delgado, H., Jankovic, J., Hunter, C., Stern, M., Tran, B., Leverenz, J., Baca, M., Frank, S., Thomas, C.-A., Richard, I., Deeley, C., Rees, L., Sprenger, F., Lang, E., Shill, H., Obradov, S., Fernandez, H., Winters, A., Berg, D., Gauss, K., Galasko, D., Fontaine, D., Mari, Z., Gerstenhaber, M., Brooks, D., Malloy, S., Barone, P., Longo, K., Comery, T., Ravina, B., Grachev, I., Gallagher, K., Collins, M., Widnell, K.L., Ostrowizki, S., Fontoura, P., Ho, T., Luthman, J., Brug, M.V.D., Reith, A.D., Taylor, P., 2011. The Parkinson Progression Marker Initiative (PPMI). Prog. Neurobiol. 95, 629–635. doi:10.1016/j.pneurobio.2011.09.005

Massey, L. A., Miranda, M. A., Zrinzo, L., Al-Helli, O., Parkes, H. G., Thornton, J. S., et al., 2012. High resolution MR anatomy of the subthalamic nucleus: Imaging at 9.4T with histological validation, 59(3), 2035–2044. http://doi.org/10.1016/j.neuroimage.2011.10.016

Mayka, M.A., Corcos, D.M., Leurgans, S.E., Vaillancourt, D.E., 2006. Three-dimensional locations and boundaries of motor and premotor cortices as defined by functional brain imaging: A meta-analysis. NeuroImage 31, 1453–1474. doi:10.1016/j.neuroimage.2006.02.004

Marburg, O., 1904. Mikroskopisch-topographischer Atlas des menschlichen Zentralnervensystems mit begleitendem Texte.

Mädler, B., Coenen, V.A., 2012. Explaining Clinical Effects of Deep Brain Stimulation through Simplified Target-Specific Modeling of the Volume of Activated Tissue. AJNR Am J Neuroradiol. doi:10.3174/ajnr.A2906

Meola, A., Yeh, F.-C., Fellows-Mayle, W., Weed, J., Fernandez-Miranda, J.C., 2016. Human Connectome-Based Tractographic Atlas of the Brainstem Connections and Surgical Approaches. Neurosurgery 1–18. doi:10.1227/NEU.0000000000001224

McIntyre, C.C., Grill, W.M., 2002. Extracellular Stimulation of Central Neurons: Influence of Stimulus Waveform and Frequency on Neuronal Output. J Neurophysiol 88, 1592–1604. doi:10.1016/S0165-0173(99)00008-9

McIntyre, C.C., Grill, W.M., Sherman, D.L., Thakor, N.V., 2004. Cellular effects of deep brain stimulation: model-based analysis of activation and inhibition. J Neurophysiol 91, 1457–1469. doi:10.1152/jn.00989.2003

Merkl, A., Neumann, W.-J., Huebl, J., Aust, S., Horn, A., Krauss, J.K., Dziobek, I., Kuhn, J., Schneider, G.-H., Bajbouj, M., Kühn, A.A., 2016. Modulation of Beta-Band Activity in the Subgenual Anterior Cingulate Cortex during Emotional Empathy in Treatment-Resistant Depression. Cereb. Cortex 26, 2626–2638. doi:10.1093/cercor/bhv100

Middlebrooks, E. H., Tuna, I. S., Grewal, S. S., Almeida, L., Heckman, M. G., Lesser, E. R., et al., 2018. Segmentation of the Globus Pallidus Internus Using Probabilistic Diffusion Tractography for Deep Brain Stimulation Targeting in Parkinson Disease. AJNR Am J Neuroradiol, 107, 64. http://doi.org/10.3174/ajnr.A5641

Miocinovic, S., Noecker, A.M., Maks, C.B., Butson, C.R., McIntyre, C.C., 2007. Cicerone: stereotactic neurophysiological recording and deep brain stimulation electrode placement software system. Acta Neurochir. Suppl. 97, 561–567.

Morel, A., 2013. Stereotactic Atlas of the Human Thalamus and Basal Ganglia. CRC Press.

Mosley, P.E., Marsh, R., Perry, A., Coyne, T., Silburn, P., 2018a. Persistence of Mania After Cessation of Stimulation Following Subthalamic Deep Brain Stimulation. J Neuropsychiatry Clin Neurosci appi.neuropsych. doi:10.1176/appi.neuropsych.17060129

Mosley, P.E., Smith, D., Coyne, T., Silburn, P., Breakspear, M., Perry, A., 2018b. The site of stimulation moderates neuropsychiatric symptoms after subthalamic deep brain stimulation for Parkinson's disease. Neuroimage Clin. doi:10.1016/j.nicl.2018.03.009

Neumann, W.-J., Horn, A., Ewert, S., Huebl, J., Brücke, C., Slentz, C., Schneider, G.-H., Kühn, A.A., 2017. A localized pallidal physiomarker in cervical dystonia. Ann Neurol. doi:10.1002/ana.25095

Neumann, W.-J., Jha, A., Bock, A., Huebl, J., Horn, A., Schneider, G.-H., Sander, T.H., Litvak, V., Kühn, A.A., 2015. Cortico-pallidal oscillatory connectivity in patients with dystonia. Brain 138, 1894–1906. doi:10.1093/brain/awv109

Neumann, W.-J., Staub, F., Horn, A., Schanda, J., Mueller, J., Schneider, G.-H., Brown, P., Kühn, A.A., 2016. Deep Brain Recordings Using an Implanted Pulse Generator in Parkinson's Disease. Neuromodulation: Technology at the Neural Interface 19, 20–24. doi:10.1111/ner.12348

Oostenveld, R., Fries, P., Maris, E., Schoffelen, J.-M., 2010. FieldTrip: Open Source Software for Advanced Analysis of MEG, EEG, and Invasive Electrophysiological Data. Comput Intell Neurosci 2011, 1–9. doi:10.1155/2011/156869

Oswal, A., Jha, A., Neal, S., Reid, A., Bradbury, D., Aston, P., Limousin, P., Foltynie, T., Zrinzo, L., Brown, P., Litvak, V., 2016. Analysis of simultaneous MEG and intracranial LFP recordings during Deep Brain Stimulation: a protocol and experimental validation. J. Neurosci. Methods 261, 29–46. doi:10.1016/j.jneumeth.2015.11.029

Pauli, W.M., Nili, A.N., Tyszka, J.M., 2017. A High-Resolution Probabilistic In Vivo Atlas of Human Subcortical Brain Nuclei. bioRxiv 211201. doi:10.1101/211201

Peisker, C., Schüller, T., Peters, J., Wagner, B., Schilbach, L., Müller, U., Visser-Vandewalle, V., Kuhn, J., 2018. Nucleus Accumbens Deep Brain Stimulation in Patients with Substance Use Disorders and Delay Discounting. Brain Sciences 8, 21–15. doi:10.3390/brainsci8020021

Pipitone, J., Park, M.T.M., Winterburn, J., Lett, T.A., Lerch, J.P., Pruessner, J.C., Lepage, M., Voineskos, A.N., Chakravarty, M.M., Alzheimer's Disease Neuroimaging Initiative, 2014. Multi-atlas segmentation of the whole hippocampus and subfields using multiple automatically generated templates. NeuroImage 101, 494–512. doi:10.1016/j.neuroimage.2014.04.054

Pollo, C., Villemure, J.G., Vingerhoets, F., Ghika, J., Maeder, P., Meuli, R., 2004. Magnetic resonance artifact induced by the electrode Activa 3389: an in vitro and in vivo study. Acta Neurochir (Wien) 146, 161–164. doi:10.1007/s00701-003-0181-4

Prodoehl, J., Yu, H., Little, D.M., Abraham, I., Vaillancourt, D.E., 2008. Region of interest template for the human basal ganglia: Comparing EPI and standardized space approaches 39, 956–965. doi:10.1016/j.neuroimage.2007.09.027

Reisert, M., Kiselev, V.G., Dihtal, B., Kellner, E., Novikov, D.S., 2014. MesoFT: Unifying Diffusion Modeling and Fiber Tracking, in: Medical Image Computing and Computer-Assisted Intervention – MICCAI 2014, Lecture Notes in Computer Science. Springer International Publishing, Cham, pp. 201–208. doi:10.1007/978-3-319-10443-0_26

Reisert, M., Mader, I., Anastasopoulos, C., Weigel, M., Schnell, S., Kiselev, V., 2011. Global fiber reconstruction becomes practical. NeuroImage 54, 955–962. doi: 10.1016/j.neuroimage.2010.09.016

Richter, E. O., Hoque, T., Halliday, W., Lozano, A. M., & Saint-Cyr, J. A., 2004. Determining the position and size of the subthalamic nucleus based on magnetic resonance imaging results in patients with advanced Parkinson disease. Journal of Neurosurgery, 100(3), 541–546. http://doi.org/10.3171/jns.2004.100.3.0541

Ruiz, M.H., Bin Hong, S., Hennig, H., Altenmüller, E., Kühn, A.A., 2014. Long-range correlation properties in timing of skilled piano performance: the influence of auditory feedback and deep brain stimulation. Front Psychol 5, 377. doi:10.3389/ fpsyg.2014.01030

Schaefer, A., Kong, R., Gordon, E.M., Laumann, T.O., Zuo, X.-N., Holmes, A.J., Eickhoff, S.B., Yeo, B.T.T., 2017. Local-Global Parcellation of the Human Cerebral Cortex from Intrinsic Functional Connectivity MRI. Cerebral Cortex 1–20. doi:10.1093/ cercor/bhx179

Schäfer, A., Forstmann, B. U., Neumann, J., Wharton, S., Mietke, A., Bowtell, R., & Turner, R., 2012. Direct visualization of the subthalamic nucleus and its iron distribution using high-resolution susceptibility mapping. Human Brain Mapping, 33(12), 2831–2842. http://doi.org/10.1002/hbm.21404

Schmidt, C., Grant, P., Lowery, M., van Rienen, U., 2013. Influence of uncertainties in the material properties of brain tissue on the probabilistic volume of tissue activated. IEEE Trans. Biomed. Eng. 60, 1378–1387. doi:10.1109/TBME.2012.2235835

Schmidt, C., van Rienen, U., 2012. Modeling the Field Distribution in Deep Brain Stimulation: The Influence of Anisotropy of Brain Tissue. Biomedical Engineering, IEEE Transactions on 59, 1583–1592. doi:10.1109/TBME.2012.2189885

Schönecker, T., Kupsch, A., Kühn, A.A., Schneider, G.-H., Hoffmann, K.T., 2009. Automated Optimization of Subcortical Cerebral MR Imaging-Atlas Coregistration for Improved Postoperative Electrode Localization in Deep Brain Stimulation. AJNR Am J Neuroradiol 30, 1914–1921. doi:10.3174/ajnr.A1741

Schroll, H., Horn, A., Gröschel, C., Brücke, C., Lütjens, G., Schneider, G.-H., Krauss, J.K., Kühn, A.A., Hamker, F.H., 2015. Differential contributions of the globus pallidus and ventral thalamus to stimulus-response learning in humans. NeuroImage 122, 233–245. doi:10.1016/j.neuroimage.2015.07.061

Setsompop, K., Kimmlingen, R., Eberlein, E., Witzel, T., Cohen-Adad, J., McNab, J.A., Keil, B., Tisdall, M.D., Hoecht, P., Dietz, P., Cauley, S.F., Tountcheva, V., Matschl, V., Lenz, V.H., Heberlein, K., Potthast, A., Thein, H., Van Horn, J., Toga, A., Schmitt, F., Lehne, D., Rosen, B.R., Wedeen, V., Wald, L.L., 2013. Pushing the limits of in vivo diffusion MRI for the Human Connectome Project. NeuroImage 80, 220–233. doi:10.1016/j.neuroimage.2013.05.078

Shin, R.K., Qureshi, R.A., Harris, N.R., Bakar, D., Li, T.P., Jafri, M.S., Tang, C.-M., 2014. Wilbrand knee. Neurology 82, 459–460. doi:10.1212/WNL.0000000000000084

Sitz, A., Hoevels, M., Hellerbach, A., Gierich, A., Luyken, K., Dembek, T.A., Klehr, M., Wirths, J., Visser-Vandewalle, V., Treuer, H., 2017. Determining the orientation angle of directional leads for deep brain stimulation using computed tomography and digital x-ray imaging: A phantom study. Med. Phys. 44, 4463–4473. doi: 10.1002/mp.12424

Sudhyadhom, A., Haq, I.U., Foote, K.D., Okun, M.S., Bova, F.J., 2009. A high resolution and high contrast MRI for differentiation of subcortical structures for DBS targeting: the Fast Gray Matter Acquisition T1 Inversion Recovery (FGATIR). NeuroImage 47 Suppl 2, T44–52. doi:10.1016/j.neuroimage.2009.04.018

Tiedt, H.O., Ehlen, F., Krugel, L.K., Horn, A., Kühn, A.A., Klostermann, F., 2016. Subcortical roles in lexical task processing: Inferences from thalamic and

subthalamic event-related potentials. Hum Brain Mapp 38, 370–383. doi:10.1002/hbm.23366

Tustison, N.J., Avants, B.B., Cook, P.A., Zheng, Y., Egan, A., Yushkevich, P.A., Gee, J.C., 2010. N4ITK: improved N3 bias correction. IEEE Trans Med Imaging 29, 1310–1320. doi:10.1109/TMI.2010.2046908

Tustison, N.J., & Avants, B.B., 2013. Explicit B-spline regularization in diffeomorphic image registration. Frontiers in Neuroinformatics, 7, 39. http://doi.org/10.3389/fninf.2013.00039

Tzourio-Mazoyer, N., Landeau, B., Papathanassiou, D., Crivello, F., Etard, O., Delcroix, N., Mazoyer, B., Joliot, M., 2002. Automated anatomical labeling of activations in SPM using a macroscopic anatomical parcellation of the MNI MRI single-subject brain. 15, 273–289. doi:10.1006/nimg.2001.0978

van Wijk, B.C.M., Pogosyan, A., Hariz, M.I., Akram, H., Foltynie, T., Limousin, P., Horn, A., Ewert, S., Brown, P., Litvak, V., 2017. Localization of beta and high-frequency oscillations within the subthalamic nucleus region. Neuroimage Clin 16, 175–183. doi:10.1016/j.nicl.2017.07.018

Vanegas Arroyave, N., Lauro, P.M., Huang, L., Hallett, M., Horovitz, S.G., Zaghloul, K.A., Lungu, C., 2016. Tractography patterns of subthalamic nucleus deep brain stimulation. Brain 139, 1200–1210. doi:10.1093/brain/aww020

Vasques, X., Cif, L., Hess, O., Gavarini, S., Mennessier, G., Coubes, P., 2009. Stereotactic model of the electrical distribution within the internal globus pallidus during deep brain stimulation. Journal of computational neuroscience 26, 109–118. doi:10.1007/s10827-008-0101-y

Vorwerk, J., Cho, J.-H., Rampp, S., Hamer, H., Knösche, T.R., Wolters, C.H., 2014. A guideline for head volume conductor modeling in EEG and MEG. NeuroImage 100, 590–607. doi:10.1016/j.neuroimage.2014.06.040

Vorwerk, J., Oostenveld, R., Piastra, M.C., Magyari, L., Wolters, C.H., 2018. The FieldTrip-SimBio pipeline for EEG forward solutions. - PubMed - NCBI. BioMed Eng OnLine 17, 413. doi:10.1186/s12938-018-0463-y

Wang, B.T., Poirier, S., Guo, T., Parrent, A.G., Peters, T.M., Khan, A.R., 2016. Generation and evaluation of an ultra-high-field atlas with applications in DBS planning. SPIE Medical Imaging 9784, 97840H–97840H–10. doi:10.1117/12.2217126

Wang, Y., Liu, T., 2015. Quantitative susceptibility mapping (QSM): Decoding MRI data for a tissue magnetic biomarker. Magnetic Resonance in Medicine 73, 82–101. doi:10.1002/mrm.25358

Weigand, A., Horn, A., Caballero, R., Cooke, D., Stern, A.P., Taylor, S.F., Press, D., Pascual-Leone, A., Fox, M.D., 2017. Prospective validation that subgenual connectivity predicts antidepressant efficacy of transcranial magnetic stimulation sites. BPS 0, 888–894. doi:10.1016/j.biopsych.2017.10.028

Weissenbacher, A., Kasess, C., Gerstl, F., Lanzenberger, R., Moser, E., Windischberger, C., 2009. Correlations and anticorrelations in resting-state functional connectivity MRI: a quantitative comparison of preprocessing strategies. 47, 1408–1416. doi:10.1016/j.neuroimage.2009.05.005

Woolrich, M.W., Jbabdi, S., Patenaude, B., Chappell, M., Makni, S., Behrens, T., Beckmann, C., Jenkinson, M., Smith, S.M., 2009. Bayesian analysis of neuroimaging data in FSL. NeuroImage 45, S173–86. doi:10.1016/j.neuroimage.2008.10.055

Xiao, Y., Fonov, V., Chakravarty, M.M., Bériault, S., Al-Subaie, F., Sadikot, A., Pike, G.B., Bertrand, G., Collins, D.L., 2017. A dataset of multi-contrast population-averaged brain MRI atlases of a Parkinson's disease cohort. NeuroImage 12, 370–379.

Yeh, F.-C., Wedeen, V.J., Tseng, W.-Y.I., 2010. Generalized q-Sampling Imaging. IEEE Trans Med Imaging 29, 1626–1635. doi:10.1109/TMI.2010.2045126

Yeh, F.-C., Panesar, S., Fernandes, D., Meola, A., Yoshino, M., Fernandez-Miranda, J. C., et al. 2018. Population-averaged atlas of the macroscale human structural connectome and its network topology. NeuroImage, 178, 57–68. http://doi.org/10.1016/j.neuroimage.2018.05.027

Yeo, B.T.T., Krienen, F.M., Sepulcre, J., Sabuncu, M.R., Lashkari, D., Hollinshead, M., Roffman, J.L., Smoller, J.W., Zollei, L., Polimeni, J.R., Fischl, B., Liu, H., Buckner, R.L., 2011. The organization of the human cerebral cortex estimated by intrinsic functional connectivity. J Neurophysiol 106, 1125–1165. doi:10.1152/jn.00338.2011

Yelnik, J., Bardinet, E., Dormont, D., Malandain, G., Ourselin, S., Tandé, D., Karachi, C., Ayache, N., Cornu, P., Agid, Y., 2007. A three-dimensional, histological and deformable atlas of the human basal ganglia. I. Atlas construction based on immunohistochemical and MRI data. NeuroImage 34, 618–638. doi:10.1016/j.neuroimage.2006.09.026

Yelnik, J., Damier, P., Demeret, S., Gervais, D., Bardinet, E., Bejjani, B.-P., François, C., Houeto, J.-L., Arnule, I., Dormont, D., Galanaud, D., Pidoux, B., Cornu, P., Agid, Y., 2003. Localization of stimulating electrodes in patients with Parkinson disease by using a three-dimensional atlas-magnetic resonance imaging coregistration method. J Neurosurg 99, 89–99. doi:10.3171/jns.2003.99.1.0089

Zalesky, A., Fornito, A., Bullmore, E.T., 2010. Network-based statistic: identifying differences in brain networks. 53, 1197–1207. doi:10.1016/j.neuroimage.2010.06.041

Zhang, D., Snyder, A.Z., Fox, M.D., Sansbury, M.W., Shimony, J.S., Raichle, M.E., 2008. Intrinsic functional relations between human cerebral cortex and thalamus. J Neurophysiol 100, 1740–1748. doi:10.1152/jn.90463.2008

Zhang, Y., Larcher, K.M.-H., Misic, B., Dagher, A., 2017. Anatomical and functional organization of the human substantia nigra and its connections. Elife 6, e26653. doi:10.7554/eLife.26653

Zilles, K., Amunts, K., 2010. Centenary of Brodmann's map--conception and fate., Nature reviews. Neuroscience. doi:10.1038/nrn2776